Virginia Tech - Wake Forest
Center for Injury Biomechanics

www.cib.vt.edu

CIB Report Number 2008-060

Far Side Final Report

PREPARED FOR

Far Side Impact Research Committee
ATTN: Ken Digges & Richard Morgan
Phone: 703-726-3543 Fax: 703-726-3530
Email: rmorgan@ncac.gwu.edu

PREPARED BY

Eric Kennedy, Joel Stitzel, Scott Gayzik,
Anthony Santago, Jill Bisplinghoff and Stefan Duma
Center for Injury Biomechanics
114 Randolph Hall
Blacksburg, VA 24061
Phone: 540-231-3945 Fax: 540-231-2953
duma@vt.edu

April 15, 2008

TABLE OF CONTENTS

Virginia Tech - Wake Forest
Center for Injury Biomechanics

www.cib.vt.edu

CIB Report Number 2004-090

Analysis of Computational Neck Models

PREPARED FOR

Far Side Impact Research Committee
Attn: Ken Digges & Richard Morgan
FHWA/NHTSA
National Crash Analysis Center
G.W. Transportation Research Institute
44983 Knoll Square
Ashburn, VA 20147
Phone: 703-726-3543 Fax: 703-726-3530
Email: rmorgan@ncac.gwu.edu

PREPARED BY

Eric Kennedy, Joel Stitzel, and Stefan Duma
Center for Injury Biomechanics
114 Randolph Hall
Blacksburg, VA 24061
Phone: 540-231-3945 Fax: 540-231-2953
duma@vt.edu

June 4, 2004

Abstract

This report presents a literature review of the latest developments in the computational modeling area of neck biomechanics for specific application to the study of carotid artery injury in far-side impacts. First, mature computer models of the head and neck are reviewed to determine the most biofidelic and versatile model available. Second, full body computational models of the human are evaluated with specific emphasis on the neck region. Due to the requirements of detailed geometry for the cervical spine and neck, as well as validation in lateral impact scenarios, two models are recommended for potential use in studying far-side impacts and carotid artery injuries. The Total Human Model for Safety (THUMS) by Iwamoto et al. (2002) and the MADYMO Detailed Neck Model by Van der Horst (2002) both offer reasonable biofidelity and the accurate geometry required for studies into the lateral impact response of the neck. However, neither model offers full modeling of the soft tissues of the neck, requiring additional materials to be added to the existing models or extraction of pertinent information from these models to be used as input parameters for a more detailed local model of neck soft tissues.

Table of Contents

1. Introduction

Cervical spine injuries can be incurred under a variety of circumstances. In the past 30 years, particular emphasis has been placed on reducing the number and severity of cervical spine injuries received by automobile accident victims and by military aviators. This report presents a literature review of the latest developments in the computational modeling area of neck biomechanics. Mature computer models of the head and neck are reviewed to determine the most biofidelic and versatile model available. Also, full body computational models of the human are evaluated with specific emphasis on the neck region. The intent of this report is to provide a detailed review of the available models so that an appropriate model can be selected to obtaining the necessary data for the specific application of studying carotid artery injuries to vehicle occupants in far-side impacts. It should be noted that this review can only focus on publicly available information regarding computational models of the neck, there is the possibility that other proprietary or other similar models of the neck are used for biomechanical modeling; however, those models are not included as they are not discussed in the open literature.

2. Mature Computational Models of the Head and Neck

2.1. Introduction to Computational Modeling

As computers became practical for studying complicated mathematical problems, researchers have employed computers to aid in the understanding of the physical phenomenon they are studying. Recent advances in computer technology have allowed the use of complex computer simulation tools in biomechanics research and offer an invaluable alternative to experiments. Once a computational model has been validated, it can be run repeatedly, allowing a detailed study of the effects of minor changes to the total system performance. It can generate data useful to the researcher for the development of injury criteria and the determination of injury risk under specific conditions. However, computational models are useless unless it is proven that they can accurately replicate results from experimental testing. There are three main types of computational simulations used today: multibody models, finite element models, and combination models where multibody and finite element models are used in parallel for computational efficiency.

2.2. Multibody Models

Multibody models are the simplest of the three computational models. In multibody simulations, rigid bodies are connected to develop a complete model of the biomechanical mechanism or structure of interest. Each of these rigid bodies may have different inertial or stiffness properties and can exert forces on adjacent rigid bodies.

Huston et al. (1978a, 1978b) developed a 3-D computational model of the head and neck for use in whiplash-type injury studies (Table 1). At the time it was the most sophisticated head-neck model available. This model uses a series of rigid bodies to represent vertebral bone, and springs and dampers to represent passive muscles, ligaments and cervical discs, resulting in a 54 degree of freedom head-neck model. This model can be used to simulate the head-neck system response to a simulated impact.

Table 1 - Computational Multibody Models

Author (Year)	Program	Loading Condition	Advantages	Limitations
Huston (1978)	Unknown	Frontal impact; Lateral impact; Rear impact	Accounts for passive muscle; Good correlation with limited validation (PMHS & volunteer)	Lumped parameters for discs/ ligaments/ muscles; Not a full body model; Needs further validation; No active muscles; No injury prediction
Deng (1987)	DYNCOMBS	Frontal impact; Lateral impact; Rear impact	Passive muscles with separate lines of action; Good correlation with flexion and lateral volunteer data	No active muscles; Not a full body model; No PMHS validation; Muscle updates required; No injury prediction
Williams (1983)	Unknown	Frontal impact; Lateral impact	Separate elements for discs/ ligaments/ muscles; Active muscles; Good correlation with frontal and lateral volunteer data	Not a full body model; No injury prediction; No PMHS validation
Jakobsson (1994)	MADYMO	N/A	Rear impact	Computationally efficient; Sufficient validation for qualitative assessment of occupant response
Bomar (1998)	Head-Spine Model (PC)	Frontal impact; Lateral impact; Rear impact; Vertical impact	Separate elements for discs/ ligaments/ muscles; Graphical user interface	Inaccurate material properties; Not validated; Not a full body model; Currently in development

Huston et al.'s (1978a, 1978b) model was validated against two experimental groups; one with Post Mortem Human Subjects (PMHS) and one with live volunteers. In practice, this model achieved "excellent agreement" between model simulations and the limited experimental data that was available. Parameters used for validation were: head angular acceleration, angular velocity and angular displacement. Considering the state of technology at the time, the model is very good, but its usefulness is limited, as it was created before well founded injury criteria had been determined.

Deng and Goldsmith (1987) developed a 3D lumped parameter model of the head-neck and upper torso for use in the DYNCOMBS software package (Table 1). Their model utilizes the Huston et al. (1978b) approach for solving the relative motion between bodies, Lagrange's form of d'Alembert's principle (Deng 1987). This model also uses passive muscle pairs. The muscles are massless, and in order to approximate muscle curvature in the neck, the muscles use 3-point lines of action. It was compared to volunteer frontal and lateral flexion experimental results and correlates well. It was speculated that most of the differences between the computational model and the experimental results can be explained from the simplified computational muscle modeling and the fact that volunteer responses include active muscle contraction. In order to gain a more biofidelic model, Deng and Goldsmith (1987) stated that muscle improvements such as the addition of the proper mass and more detailed geometry should be the focus of future investigations.

Williams and Belytschko (1983) created another 3D rigid body model of the cervical spine (Table 1). Rigid bodies of vertebrae are connected by deformable elements representing the discs, facet joints, ligaments and muscles. Unlike Huston et al.'s (1978a, 1978b) model, Williams and Belytschko created their model with curved musculature which could

be left to operate passively or set to respond actively after a certain time of 40 to 100 ms into the simulation. Overall, the simulations show that active muscle behavior can have a great influence on model behavior compared to passive muscles only. This model was validated for frontal and lateral impacts and good correlation with volunteer experimental data validate the active muscle behavior modeling of the computer simulation.

Jakobsson et al. (1994) developed a MADYMO model for use in studying occupant performance in rear-end collisions (Table 1). However, this model is a greatly simplified two-dimensional rigid body model. As the item of interest was a study of "whiplash" type trauma, the spine is modeled by a series of rigid bodies. The model was validated against a limited series of rear-end volunteer simulations and determined to be biofidelic enough for a qualitative assessment of occupant response in rear-end impact scenarios. The forces best correlated to risk of injury were tensile and shear forces between vertebrae, head angular acceleration, and volume rate of change of the cervical spinal canal (Jakobsson 1994). Because it is a two-dimensional model, it is not of use for studying lateral impacts.

The most recent multibody model developed for neck injuries is the U.S. Air Force Head Spine Model by Bomar and Pancratz (1998) (Table 1). The model is an update of an existing Air Force Head Spine Model, so that it may be run on a personal computer platform. The model consists of rigid inertial elements with massless deformable elements to represent muscles, ligaments, cartilaginous joints and other connective tissues. According to Bomar and Pancratz (1998), data for some of the element properties of the original Head Spine Model are several orders of magnitude different than currently available material property data. These discrepancies were not corrected during this particular revision, as the focus was on programming the existing Head Spine Model for use on a modern computer platform. In addition to corrections of element properties, recommended updates by the creators include more realistic muscles and intervertebral-discs as well as more accurate assumptions of the static tension in cervical ligaments. Future updates will allow the addition of rigid bodies to the existing model and will include injury estimate processing capabilities (Bomar 1998).

The Bomar and Pancratz Head Spine Model is still in development, but it promises to have good potential for head-spine work. The model discussed has not been validated, to date, and does not utilize the latest published material properties, nor does it have the capability to allow additions of other rigid bodies to an existing model. Other multibody models have been developed for studying specific impact loading conditions on the neck; however, they do not have significantly different features than the models already discussed (Bosio 1986, Bowman 1972, Bowman 1975, Bowman 1981, Bowman 1984, Goldsmith 1984, Li 1991, McElhaney 1979, Melvin 1972, Nightingale 2000, Paver 1990, Seemann 1984, Tien 1985, Tien 1987).

2.3. Finite Element Models

Finite Element (FE) models are more complicated than the multibody models and require more computational time, but can provide more detailed information than multibody

models. In FE modeling, the geometry of a body is defined and broken down into a discrete grid of elements. Stresses and strains can be calculated within elements and localized regions of stress and strain can be determined. Forces or accelerations can then be exerted on the model, to pinpoint the areas where stress and strain may be high. The disadvantage of this type of modeling approach is that it is not as computationally efficient as multibody modeling and thus simulations cannot be run as quickly or in as many configurations as easily as with a multibody model.

LS-DYNA was used by Kleinberger (1993) to develop a 3D model of the cervical spine (Table 2). To increase its accuracy, this model needs additional musculature, improvements to soft tissue material properties and refined geometry. At the time, run times were up to 20 hours in duration per simulation for a cervical spine model only. The model was given only a limited validation against a set of published experimental data. It was stated that testing was underway to provide experimental data for further development and validation, but more recent publications discussing this model are not presently available.

Table 2 - FE Model Summary

Author (Year)	Program	Number of Elements	Loading Condition	Advantages	Limitations
Kleinberger (1993)	LS-DYNA	1600 Solid/ Vertebrae	Frontal impact; Lateral impact; Rear impact	Uses published material properties; Detailed mesh geometry	No musculature; 20 hour runtime; Not validated; Not a full body model; No injury prediction
Dauvilliers (1994)	RADIOSS	150 Solid; 104 Shell; 412 Damping-spring	Frontal impact; Lateral impact	Good correlation with volunteer data on initial impact; Computationally efficient; Integrated with FE full body model; Global injury prediction in full body model	No musculature; Poor correlation with volunteer data after initial impact; No PMHS validation; Full body model intended to represent 60 year old male
Nitsche (1996)	PAM-CRASH	1852 Solid; 86 Membrane	Frontal impact; Lateral impact; Axial impact	Good correlation with PMHS and volunteer data	No musculature; Not a full body model; No injury prediction
Yang (1998)	PAM-CRASH	11,498 Solid; 3071 Shell-membrane	Frontal impact; Rear impact; Axial impact	Detailed geometry; Passive muscles included	More validation required; Not a full body model; 3-24 hour runtime
Deng (1999/2002)	LS-DYNA	Unknown	Frontal impact	Detailed geometry; Active muscles; Good correlation with low-severity frontal impact	Not a full body model; More validation required; Enhancement of material models needed
Halldin (2000)	LS-DYNA	4560 Solid; 3572 Shell; 230 Spring	Axial impact	Able to predict injury from compressive impact	No musculature; Transverse processes not included on vertebral bodies; Not a full body model; Limited loading conditions; 45 hour runtime

Another FE model of the human neck was developed by Dauvilliers et al. (1994) using RADIOSS software (Table 2). The model was developed for use in frontal and lateral impacts. The developers modified ligament stiffness in an attempt to include passive neck muscles in the model, as they were thought to affect dynamic behavior of the head and

neck (Lizee 1998). The FE neck was then integrated into a 50th percentile seated male FE model by Lizee et al. (1998). The goal was to have a full body FE model of a seated male. However, the model needs more development to predict injury risks (Lizee 1998). Dauvilliers et al. (1994) also noted that more realistic passive muscle action is needed in future versions of the model, for a more biofidelic response.

Nitsche et al. (1996) developed a FE model of the spine utilizing PAM-CRASH software (Table 2). This model is of the cervical spine only, and it does not contain active or passive muscles. Such a basic model, however, illustrates a problem with current FE models of the head and neck region. Since local parameters such as max stress and strain are unknown for the cadaver and volunteer validation tests, the model cannot be validated against its calculated output. The model was validated against global motion of the neck with the assumption that if the global motion is correctly simulated, the local stresses and strains of local tissue must be reasonably accurate, and are therefore validated (Nitsche 1996).

Nitsche's (1996) model was validated by comparing to published experimental data of frontal flexion, lateral flexion, and compression of the spine in both volunteer and cadaver experiments. Experiments of both frontal and lateral flexion were compared to the PAM-CRASH model's displacement of the occipital condyles and the center of gravity of the head relative to a non-rotating T1, in order to determine the relative rotation angle of the head. Comparison of the simulation's output to the experiments show that the FE model motions displays acceptable agreement with test results in frontal flexion, but less agreement in lateral flexion (Nitsche 1996). In order to gain more realistic biofidelity and usefulness, this model needs to be enhanced with musculature and integrated into a head-upper torso system.

A recent 3D FE model of the neck was developed by Yang et al. (1998) using PAM-CRASH software (Table 2). This model is a full FE version of the head and neck, which can be incorporated into an upper torso model. The intended application of this model is to study the neck loads experienced as an occupant comes in contact with an airbag. This model includes passive muscle modeling only, with no active muscle response. This model is very computationally intensive as it requires 3-24 hours on a Cray supercomputer to run one simulation. For initial validation this model has been compared to a limited amount of cadaver tests with encouraging results; however, this model needs more validation against experimental data before it can be fully utilized. Also, reductions in run times or advances in computer technology need to be made to maximize this model's usefulness.

Deng et al. (1999) developed a LS-DYNA FE model of the neck with detailed 3D anatomical data (Table 2). This model contains detailed intervertebral discs with both the nucleus pulposus and the annulus fibrosis, neck ligaments, and detailed 3D representations of the vertebral bodies. All material properties used for the model are based on numerical analysis of existing published data. Although the vertebral bodies are modeled with elastic-plastic material properties, all validation work on the model has treated the vertebral bodies as rigid materials. An update of this model added neck musculature to the FE model (Deng 2002). The muscles are modeled as Hill-type elements and allow for active muscle generation. The updated model with muscles was validated against published low-

severity frontal crash volunteer studies. The model displays good general agreement with the volunteer tests once the muscle activation schemes have been optimized.

A 3D FE model of the neck was developed by Halldin et al. (2000) to study compression injuries of the neck (Table 2). This model runs in the LS-DYNA software environment and utilizes 4560 solid elements, 3572 shell elements and 230 spring elements to model the cervical vertebrae, ligaments and discs. Since neck musculature is not thought to greatly influence neck response on compressive impacts, neck musculature and the corresponding transverse processes of the vertebral bodies are omitted from this model. This model was validated to axial impacts of the head and was found to be able to predict injury by local stress of neck tissues; however, at certain impact angles the model predicted failures where none were experienced in the corresponding experimental test. This model has not been validated for any other type of impact situation, nor have the authors mentioned intent to further develop the model for other loading scenarios.

Other FE models have been developed to study specific impact loading conditions on the neck. However, they do not have better features than the models discussed previously (Frechede 2003, Roychoudhury 2000, Yang 1992, Yoshida 2002).

2.4. Multibody-Finite Element Combination Models

Perhaps the most effective method to study a particular region on a large scale model, multibody-FE combination models allow the user to model the area of interest with FE techniques and other global regions with computationally efficient multibodies. Several software packages allow this option, with LS-DYNA and MADYMO being among the most commonly used.

Camacho et al. (1997) created an LS-DYNA model of the cervical spine and head (Table 3). The intended use of this model is to simulate spinal behavior for “near-vertex” (+/-15 degrees of head vertex with torso) head impacts (i.e. compressive forces). To this effect, the attached head is modeled as a deformable FE head with rigid body vertebra. Like many of its computational predecessors, this model has no neck musculature. According to the authors, this is because musculature is not thought to be able to react fast enough to affect the response of the neck under compressive impacts (Camacho 1997). The authors also assert that due to the lack of data available on dynamic material properties, many of the material properties had to be inferred. It is for this reason that it makes sense to use a more computationally efficient lumped or rigid body model, that does not rely completely on material properties to determine accurate three-dimensional kinematics. Also, they state that material-based tolerance criteria lack injury correlation with predicted stresses and strains.

Table 3 - Multibody-Finite Element Combination Models

Author (Year)	Program	Number of Elements	Loading Conditions	Advantages	Disadvantages
De Jager (1996)	MADYMO	N/A	Frontal impact; Lateral impact	Active muscles; Detailed geometry; Good correlation with frontal and lateral volunteer and PMHS data	Unrealistic muscle lines of action; Less sophisticated than Van der Horst model
Camacho (1997)	LS-DYNA	639 Rigid; 448 Deformable	Axial impact	Good correlation with axial loading cadaver data; Computationally efficient	No musculature; 3-24 hour runtime; Not fully validated; Not a full body model
Van Ee (2000)/ Chancey (2003)	LS-DYNA	639 Rigid; 448 Deformable	Axial impact	Active muscles; Good correlation with axial loading cadaver data	Not fully validated; Not a full body model
Van der Horst (2002)	MADYMO	N/A	Rear impact; Frontal impact; Lateral impact	Good correlation with frontal, lateral and rear impact volunteer and PMHS data; Refined geometry over De Jager model; Active muscles; Detailed for local and global injury assessment	FE techniques would offer better local injury assessment; Lack of high severity muscle activation data

The Camacho model was updated by Van Ee et al. (2000) to include neck musculature (Table 3). This update added 24 muscle pairs to the model via spring elements. The muscle response characteristics are based upon the physiologic cross-sectional area of the muscles in the cervical spine. Basing the muscle response characteristics on the size of the muscle and incorporating detailed lines-of-action of the individual muscles is thought to provide the most physiologically accurate estimation of each muscle's contribution to the motion of the cervical spine. The muscles were also modeled such that they could be actively controlled in the simulation. The model was only validated to tensile neck testing and the active effect of the muscles was shown to move the site of injury typically seen at the lower cervical spine in experimental cadaver work, to the upper region of the cervical spine where most clinical cases of spine injury are observed. This model was again updated by Chancey et al. (2003) to determine the state of active musculature required to maintain the head in an initially stable, upright position. A common problem with active musculature modeling is that the head is not initially stabilized, due to the effects of gravity, prior to the crash event. This model was used to more accurately estimate the tensile neck tolerance of the cervical spine, though it has not been validated to other loading scenarios.

The most current detailed neck model, created in MADYMO, was completed by Van der Horst (2002). The Van der Horst (2002) model is a major update of the MADYMO head-neck model developed by de Jager (1996a, 1996b). The de Jager model traces its heritage back to the previously discussed three-dimensional head-neck multibody model of Deng and Goldsmith (1987). In order to develop a detailed head and neck model for the MADYMO software package, de Jager adapted Deng and Goldsmith's 3D head and neck model (Table 3). De Jager preferred to use a more simplistic model than a FE model, since FE models are very complex, computationally inefficient and difficult to validate with so many parameters. Therefore, the model was implemented as a discrete parameter model

with multiple rigid bodies of 3D global mesh geometry, from which the complexity could be increased as the model was validated. De Jager intended that a computationally efficient, validated model, the end result would be more practically useful than an FE model, since material properties of the human neck are not fully known (de Jager 1994).

The de Jager model offers fair agreement for frontal impact, its inaccuracies attributed to inappropriate modeling of AOC joint. Reasonable to excellent agreement with experimental results are found with lateral impacts (de Jager 1994, de Jager 1996a). Results from de Jager's model show that head rotation in this model is too large, most likely as a result of inadequately stiff muscles. Comparing to PMHS experiments, the "cadavers show a similar difference in response with the volunteers as the model, indicating that muscle tensioning limits head rotation and prevents overtipping for the volunteers" (de Jager 1994).

De Jager's (1996b) detailed neck model also includes the capability to simulate active muscle control. Fourteen pairs of Hill-type elements are used as muscles in the detailed model. De Jager also developed a global model, which has lumped parameters for discs, ligaments, facet joints and muscles. While certainly more detailed than the global model, the muscles in the detailed model are still not completely representative of anatomical geometry. The muscles in the detailed model are not curved, and are attached only to an average vertebrae position (de Jager 1996a). The inclusion of neck musculature means that modifications to neck strength can be made by changing parameters characterizing the muscles. Also, due to the increased anatomical description of the neck in the detailed model, the user has the ability to determine loads and deformation of individual soft tissue within the neck (de Jager 1996a). Several "next steps" were identified by de Jager for future improvements for an even more refined model. These recommendations include a more detailed intervertebral joint, separate representations of soft tissue, and more refined geometry, including an increase in the detail of the neck musculature (de Jager, 1994). Attempts to improve the de Jager model were carried out by Yamazaki et al. (2000) and Brelin-Fornari (1998); however, the updates were not as significant as a more recent update.

A major update of the De Jager model was performed by Van der Horst (2002) (Table 3). The Van der Horst model, like the De Jager model, includes rigid bodies as vertebrae but includes more detailed geometry of facet joints and ligaments, as well as anatomically accurate, curved neck muscles. Although the MADYMO software program is capable of FE modeling, the Van der Horst model only uses multi-body techniques (Van der Horst 2002). Van der Horst's model uses Hill-based muscles, which are currently the most widely used and accepted mathematical adaptation of a muscle (Van der Horst 2002, Winters 1990a). In de Jager's neck model, the neck muscles are modeled by cord elements connecting the muscle attachment points. Van der Horst added significantly more detail to the neck muscles as the cord elements do not accurately simulate active neck muscles (Van der Horst 2002). Multi-segment muscles were added to allow for curvature of neck muscles and therefore more realistic lines of muscle action (Happee 1999, Van der Horst 2002).

Van der Horst's neck model has been incorporated into a larger, full body human model (Happee 1999, Van den Kroonenberg 1997). The intent was to create a biofidelic MADYMO human body model for use in a variety of omnidirectional computer simulations. Once validated, experiments can be conducted using either dummies or cadavers and correlated to the computer model of the human subject using active muscles. A validated computer model that could easily be modified would be useful to study aspects like body size, posture, muscular activity and post fracture response (Happee 1999). Also, the computer model anatomy is detailed enough, despite the lack of FE deformation, that it can give insight into injury mechanisms on a tissue level (Happee 1999). In 2000, Happee et al. published a paper on two recent MADYMO models, a small female and mid size male. The Van der Horst detailed head-neck model is used only in the mid size male model. However, the male model has been widely validated using frontal volunteer sled tests, frontal and lateral PMHS impactor tests, lateral PMHS sled tests, and rearward volunteer and PMHS tests (Happee 2000).

The Van der Horst model was used for extensive testing in rear-end impact simulations and gave very encouraging results (Van der Horst 2001) (Table 4). Data shows more realistic responses with stiff passive muscles than with normal passive muscles, except for head center of gravity x-displacement which shows too little x-displacement. Therefore, it is logical that for future work, the stiff muscles be used to obtain a more accurate biofidelic solution (Van der Horst 2001).

Table 4 – Biofidelity of Stiff Passive Muscle Response in MADYMO Detailed Human Neck Validation Tests (Van der Horst 2001)

Good (in envelope)	Reasonable (<25% outside envelope)	Poor (>25% inside envelope)
Head rotation (stiff muscles)	T1 Rotation	T1 Z-displacement
Head CG x-displacement (normal muscles)	T1 X-displacement	Head CG acceleration (>100ms)
Head CG z-displacement (stiff muscles)	Head rotation (normal muscles)	
Head CG z-acceleration	Head CG x-displacement (stiff muscles)	
Head CG angular acceleration	Head CG z-displacement (normal muscles)	
	Head CG acceleration (initial)	

Van der Horst's model was also validated against volunteer data for frontal crashes from 2 g to 15 g. Muscle contraction shows a large influence on the head-neck response. Wismans et al. (1998) describes high severity frontal crash simulations with PMHS. In testing, it is noted that head center of gravity trajectories are of the same order of magnitude as lower severity volunteer experiments, but the head rotations are larger in the PMHS. This is attributed to the fact that the PMHS do not benefit from the active muscle control that volunteers in low severity testing are able to display (Wismans, 1998). Similarly, as suggested by the volunteer and PMHS experiment comparisons, it is noted in

testing of Van der Horst's model that muscle contractions have a large effect on the head-neck response (Wismans 1998).

In a 15 g frontal simulated crash volunteer test, it is found that the Van der Horst model with active muscles predicts accurate head-neck response in terms of trajectories, head rotation and head lag. In the same testing, it is noted that angular and resultant head acceleration are largely unaffected by active muscle response (Wismans 1998). For this reason, the authors conclude that acceleration data may not be a good indicator of true biofidelity in a model. This may also mean that injury criterion such as the Neck Injury Criterion (NIC), will not be affected by active muscle response, since it is based in large part on head acceleration.

In lower severity simulations, in order to achieve realistic performance of the simulation compared to the volunteer experiments, a lower activation level of the muscles and a larger reflex delay may be required (Wismans 1998). Similarly, the influence of the muscles on the occupant simulation increases with the muscle activation level (Van der Horst 1997). By this reasoning, it can be speculated that the effect of muscles during severe impacts is not yet fully understood. Since volunteer testing is limited to low severity testing, muscle activation in high severity impacts has not been fully tested. Computer simulations may offer the greatest insight into this phenomenon if data can accurately be extrapolated for full muscle activation.

Wismans et al. (1998) concluded that the Van der Horst model with fully activated muscles lies almost entirely within response corridors developed by both PMHS and volunteer experiments for frontal impact scenarios. This computer model was also determined to be more biofidelic than both the THOR and Hybrid III Anthropomorphic Test Devices (ATDs). Further validation of the Van der Horst model was conducted by Van Hoof (2002) and was found to correlate well with volunteer test data.

Lateral validation tests were performed for the Van der Horst model by Meijer et al. (2003). In these tests, volunteer responses to low severity lateral impacts were recorded and head kinematics were used to validate the simulation output. By varying the levels of muscle activation to between 50 percent and 100 percent activation the model displayed good correlation to the head kinematics measured by the volunteers. These validation experiments were performed with only two volunteers, so further validation work is planned for lateral impacts, although initial results have shown to be promising.

Seating posture was also varied by Van der Horst for evaluation of the effect of occupant positioning on neck response. From the outcome of the studies, it was shown that initial posture has a large influence on the head-neck motions (Van der Horst 2001, Van der Horst 2002). Therefore, it is imperative that proper positioning of the occupant be considered before running the simulation. Also, likely out-of-position scenarios should be evaluated to determine if they represent a significant risk of injury beyond the normal "in-position" crash sequence.

Other multibody-FE combination models have been developed for studying specific impact loading conditions on the neck; however, they do not have features other than those already discussed (Hayamizu 1999, Weerappuli 1998).

2.5. Computational Model Summary

Computer models have been used to better understand the human head-neck system kinematics since the 1970's. Although favorable correlation was found even then, computer models of today display a great deal of biofidelity and offer versatility and repeatability not possible experimentally.

Finite Element models are capable of providing detailed information regarding localized loading conditions and predicting high stress or strain areas. FE models are also very computationally intensive, requiring longer amounts of computing time per simulation. Multibody models, however, are more computationally efficient than FE models, and can offer biofidelic responses on par with current FE element models but without details of local stresses and strains. Additionally, multibody-FE combination programs, such as MADYMO, allow users the versatility to choose between computational efficiency and generation of detailed localized analysis. They allow the user the option to develop a multibody model, which can be modified later if material properties are not known, or if more detailed output is desired.

Van der Horst (2002) has developed the most widely validated head-neck model using the MADYMO computational simulation program. This model has the capability of simulating active muscle response, which sets it apart from other models available today. Due to the lack of available information on all material and failure properties of the neck, developers of FE models are forced to iterate material property values until they reach dynamic correlation with volunteer and PMHS experiments. Therefore, the Van der Horst detailed neck model loses very little in terms of output, but offers a great deal in its validation and active muscle features. Specifically concerning detailed neck models, it is currently the model of choice to use in a computational simulation of neck response to dynamic loading conditions.

3. Full Body Human Models

3.1. Introduction to Full Body Models

For the purposes of studying carotid artery injuries to far-side occupants, it is necessary to not only have a detailed model of the neck, but also to have a full body model of the occupant. These full body models will allow the researcher to study the interaction of the neck with the shoulder belt and kinematics of the head, which alone or in combination are commonly thought to be mechanisms for injury for the carotid artery. Many of the models discussed include detailed models of the neck from the previous section; however, the purpose of this portion of the paper is to provide an overview on the different full body models that have been presented in the recent literature.

3.2. Multibody Models

Although there are many full body multibody models of the human occupant available in the literature, their usefulness is limited, given the availability of FE and Multibody-FE combo models with detailed models of the neck. Therefore, no multibody ellipsoid models were evaluated for their usefulness for this project.

3.3. Finite Element Models

There are several projects underway to develop a useful FE model of the whole human body. The advantage to this technique is that it provides a platform that can be theoretically used in a multitude of crash or impact scenarios, if the model is carefully constructed to offer accurate replication of the structure of the human body.

As mentioned previously, the component FE model of the neck developed by Dauvilliers et al. (1994) was integrated into a seated occupant model by Lizee et al. (1998). This full body model was intentionally kept geometrically simple, as it was intended for use in full vehicle models and it was not desired that the addition of the occupant would adversely affect the run time of the simulation. The model size was limited to 10,000 elements; however, even with its inherent simplicity the model was able to accurately predict occupant responses to frontal, lateral, and some rear impact scenarios. The model does not have enough detail, in current form, to predict injury to specific regions of the body; however, with detailed improvement it should not only be able to predict accurate kinematics but also localized loads of tissues.

A model referred to as the H-Dummy was presented by Choi et al. (1999). The model is intended to provide an omni-directional model that can be used in a variety of impact situations. The model contains a detailed cervical spine with vertebrae, ligaments, discs and muscles. Geometric data incorporated into the model was based on Viewpoint Datalabs' dataset and various anthropometric textbooks. No discussion is given to the

selection of material properties or the active/passive response of the muscle models. The cervical spine motion was validated both to local response of each pair of adjacent vertebrae and global response of the neck, to previously published data. Additional data was published by Choi et al. (2002) validating the response of the model specifically to low speed rear impacts.

Another FE model of the human occupant is the Total Human Model for Safety (THUMS) (Iwamoto 2002). This model presents a FE model of the bones, ligaments, tendons, flesh, and skin, there are also detailed models of the shoulder, head and face, or internal organs, if those are of interest for the simulation. As in the H-Dummy, geometric data was taken from Viewpoint Datalabs and anatomy textbooks. The neck muscles can be flexed to simulate active musculature; however, they are tension only members utilizing bar elements. The thorax and spine segments of the model have been validated for side impacts and are reported to fall within published cadaver response corridors. With approximately 83,500 elements, the base model runs with a minimal amount of CPU time and is able to simulate detailed injuries to the cervical spine and thorax.

Ford Motor Company has been developing a FE human body model that operates in the PAM-CRASH environment (Ruan 2003). The model consists of approximately 103,000 nodes and 119,000 elements. Geometry of the model is based on the Visible Human Project and anatomical texts and incorporates an updated version of the neck model previously developed by Nitsche et al. (1996). Originally validated by Nitsche, the model has been further elaborated with new facet joints along with new and remodeled ligaments. At present, the integrated neck model has not been validated in lateral impacts, although in component testing, the original neck model (Nitsche 1996) was validated to frontal, lateral and rear impact scenarios. As discussed previously, in those validation tests the head-neck motion was compared to that from frontal and lateral volunteer tests and displayed better correlation with frontal test data than with lateral test data. It is unknown whether the improvements the model have improved the lateral impact response. The integrated full body model has been validated to lateral thoracic impact.

Currently, such an effort is underway at Wayne State University, to develop an advanced FE model of the human (Yang 2003). The model is a combination of human component models that have been developed based on the scale of a 50^{th} percentile male. This model incorporates the detailed neck model presented by Yang et al. (1998), which was discussed previously. Geometric data for the neck model comes from an MRI of an approximate 50^{th} percentile male individual, other geometry is taken from the Visible Human Project. The neck model incorporates detailed geometry of the neck, passive muscle bar elements, and intervertebral discs; however, the model does not yet have the capability for active muscle simulation. The fully developed and integrated model is expected to be completed sometime in the next five years.

Lastly, a human body model consisting of the THUMS and Engineering Systems International's H-Dummy (Murakami 2004). The upper body of this integrated model is taken from THUMS, while the lower extremities of the model are developed from the H-model. This model contains approximately 67,000 nodes and the geometry of the vertebrae

are accurately modeled using rigid body solid elements. As this model's thorax, head, and neck originated from the THUMS model, it can be assumed that geometry originated from Viewpoint Datalabs and anatomical text, although details of further geometrical refinement are not offered. Intervertebral discs are modeled as deformable solid elements and cervical ligaments are modeled as membrane elements. Muscles consist of active and passive Hill-type elements. Neck response of this model was compared to a volunteer whiplash simulation where good correlation was seen in the initial phase of motion, until maximum extension; however, the motion after the maximum extension did not correlate with the human volunteer responses. Further work is necessary to optimize the head-neck responses of this model to impact scenarios, with possible improvements coming in the form of soft tissues of the neck and improved muscle element modeling.

3.4. Multibody-Finite Element Combination Models

As mentioned previously, a full body human model with a detailed neck exists in the MADYMO software environment (Happee 1999, Van der Horst 2002). This model contains the detailed neck model developed by Van der Horst (2002) which is a rigid-body model utilizing detailed geometry of facet joints and ligaments, as well as anatomically accurate, curved neck muscles. Geometry was defined by dissection of a frozen cadaver in a seated automotive posture. No FE techniques are currently employed in the MADYMO full body model with integrated detailed neck. MADYMO is capable of performing FE simulations and a FE human model does exist; however, the geometry of the cervical spine is less detailed in the FE human. Also, as mentioned previously, lateral impact validation has been performed using the MADYMO detailed neck model (Meijer 2003). Although validation tests were compared to a small number of physical experiments, the model showed good overall correlation to the limited number of tests.

3.5. Full Body Model Summary

The ability to duplicate the positioning of the occupant in the vehicle and replicate the total response of the occupant in an impact, including interaction with the restraint system is the main advantage the full body models offer over the component neck models. When using a component model, it is necessary to understand the orientation and constraints of the whole body so that the component model can be setup in a life-like scenario; however, the use of a full body model allows a more intuitive model setup, with an occupant's position and restraint systems mimicking the physical setup. In the last several years, the level of detail in full body models has begun to approach that originally seen only in component level models. As a result, the use of a full body models to gain information on loads and kinematic responses seen by the occupant is becoming more and more prevalent. The individual full body models reviewed in this chapter will certainly help the researcher understand the biomechanics of impact to a greater level of detail then ever before; however, each model presents its own advantages and disadvantages (Table 5).

Table 5 – Summary Table of Full Body Models

Author (Year)	Program	Number of Elements	Loading Conditions[1]	Advantages	Disadvantages
Lizee (1998)	RADIOSS	10,000 elements	Frontal impact; Lateral impact; Rear impact	Computationally efficient; Good global validation	Rudimentary geometry; No neck musculature; Lack of detail for interpretation on local tissue level; No soft tissue modeling around neck
Choi (1999)	PAM-CRASH	Unknown	Rear impact	Some soft tissue modeling of vertebrae, muscles, ligaments, organs, discs, and fatty tissues in neck and torso	Only validated to low speed rear impacts; Unknown level of detail of soft tissue in neck
Iwamoto (2002)	PAM-CRASH/ LS-DYNA	83,500 elements	Frontal impact; Lateral impact; Rear impact	Thorax and spine segments of model validated for lateral impacts; Active neck musculature	Lacks overall validation of complete model; No soft tissue modeling around neck
Ruan (2003)	PAM-CRASH	103,000 nodes; 119,000 elements	Frontal impact; Lateral impact; Rear impact	Detailed neck model with new and remodeled facet joints and ligaments	Lacks overall validation of model; No neck musculature; No soft tissue modeling around neck
Yang (2003)	PAM-CRASH	Unknown	Rear impact; Frontal impact	Marriage of separate detailed component models (head, neck, thorax, abdomen, lower limb)	Incomplete; No active musculature; No soft tissue modeling around neck
Murakami (2004)	UNKNOWN	67,000 nodes	Rear impact	Optimized mesh quality and calculation time (over THUMS and H-Dummy contributors); Active neck muscles	Low level validation; No soft tissue modeling around neck
Van der Horst (2002)	MADYMO	N/A	Rear impact; Frontal impact; Lateral impact	Good correlation with frontal, lateral and rear impact volunteer and PMHS data; Refined geometry over De Jager model; Active neck muscles; Detailed for local and global injury assessment	FE techniques would offer better local injury assessment; Lack of high severity muscle activation data; No soft tissue modeling around neck

[1] All of these models are intended for ultimate use in any loading direction. Loading conditions presented here are for impact directions that neck component has been subjected to.

These models presented are all in various states of development and have undergone various states of validation. For the specific purposes of studying far-side impacts, the best choice of models from those available would be one that has had extensive development and validation to lateral impacts. With that in mind, several models should likely be omitted from lateral impact studies in their current form. Although no models have provided extensive validation data for lateral impacts, the Iwamoto et al. (2002) and Van der Horst (2002) models have seemingly had the most development for lateral impact scenarios. The Van der Horst model has been globally validated to a limited number of lateral scenarios and has displayed reasonable agreement, although to a small sample size of validation tests. The Iwamoto model has not been globally validated to lateral impacts; however, the thorax and spine segments of the model have been validated to lateral impacts. Since these are likely the most important areas of the body for studying carotid artery injury, it is felt that this model will have sufficient biofidelity in its current state for these types of simulations.

4. Conclusion

Despite the obvious complexities of the human body, it has been shown that a myriad of computational models of the neck exist. The level of detail in the models presented in the literature varies widely, from low level detail offering rudimentary kinematic correlation, to highly detailed models with accurate geometry and simulation of active muscle control. For the purposes of studying the effects of injuries to the carotid artery for occupants on the far-side of the struck vehicle, it is necessary to have a detailed understanding of the kinematics of the neck under lateral impact and to understand the local loading mechanisms of the tissues of the neck, preferably with a detailed understanding of geometrical interactions. It is difficult to make a judgment on which model has the most accurate anatomical data, but it can be said that the nodal makeup and mesh size of even the most finely meshed model in this review is quite large compared to what would be required for accurate modeling of the tissue of the carotid artery itself. Considering that a co-requirement to accurate geometry is that the model is validated for lateral impacts, the two most possibly useful models are the THUMS model by Iwamoto et a. (2002) and the MADYMO model by Van der Horst (2002). Both of these models will be able to provide the most accurate representation both globally and locally of the kinematics of the neck under lateral bending; however, both of these models are limited in that they do not fully represent the soft tissues around the neck, rather incorporate major tissues such as the bony structures, discs, and ligaments, while representing the muscle lines of action. Aside from a shroud of skin mesh around the models, no localized interactions with soft tissues such as fat or perturbation of the muscles are accounted for. However, these models contain sufficient features that can be monitored during simulations to extract meaningful data for validation of a more specialized local model of the cervical neck with accurate soft tissue representations.

References

Bomar, J.B., and Pancratz, D.J. (1998) A PC-Based Head-Spine Model. NATO RTO Meeting Proceedings 20; Models for Aircrew Safety Assessment: Uses, Limitations and Requirements: 4-1-4-11 North Atlantic Treaty Organization Research and Technology Organization.

Bosio, A.C., and Bowman, B.M. (1986) Simulation of Head-Neck Dynamic Response in –Gx and +Gy. Stapp Car Crash Journal 30: 345-378. SAE 861895.

Bowman, B.M., and Robbins, D.H. (1972) Parameter Study of Biomechanical Quantities in Analytical Neck Models. Stapp Car Crash Journal 16: 14-44. SAE 720957.

Bowman, B.M., and Schneider, L.W. (1975) Simulated Occupant Response to Side-Impact Collisions. Stapp Car Crash Journal 19: 429-454. SAE 751155.

Bowman, B.M., Schneider, L.W., Rohr, P.R., and Mohan, D. (1981) Simulation of Head/Neck Impact Responses for Helmeted and Unhelmeted Motorcyclists. Stapp Car Crash Journal 25: 13-68. SAE 811029.

Bowman, B.M., Schneider, L.W., Lustick, L.S., Anderson, W.R., and Thomas, D.J. (1984) Simulation Analysis of Head and Neck Dynamic Response. Stapp Car Crash Journal 28: 173-205. SAE 841668.

Brelin-Fornari, J.M. (1998) A Lumped Parameter Model of the Human Head and Neck with Active Muscles. PhD thesis, University of Arizona, USA.

Camacho, D.L., Nightingale, R.W., Robinette, J.J., Vanguri, S.K., Coates, D.J., and Myers, B.S. (1997) Experimental Flexibility Measurements for the Development of a Computational Head-Neck Model Validated for Near-Vertex Head Impact. Stapp Car Crash Journal 41: 473-486. SAE 973345.

Chancey, V.C., Nightingale, R.W., VanEe, C.A., Knaub, K.E., and Myers, B.S. (2003) Improved Estimation of Human Neck Tensile Tolerance: Reducing the Range of Reported Tolerance Using Anthropometrically Correct Muscles and Optimized Physiologic Initial Conditions. Stapp Car Crash Journal 47. SAE 2003-22-0008.

Choi, H.Y., Eom, H.W., Kho, S.T., Lee, I.H. (1999) Finite Element Human Model for Crashworthiness Simulation. SAE 1999-01-1906.

Choi, H.Y., Lee, I.H., Haug, E., and Lee, J.H. (2002) Finite Element Human Model for Low Speed Rear Impact Situation. Proc. of the 2002 World Congress of Biomechanics.

Dauvilliers, F., Bendjellal, F., Weiss, M., Lavaste, F., and Tarriere, C. (1994) Development of a Finite Element Model of the Neck. Stapp Car Crash Journal 38: 77-91. SAE 942210.

Deng, Y.C., and Goldsmith, W. (1987) Response of a Human Head/ Neck/ Upper-Torso Replica to Dynamic Loading – II. Analytical/ Numerical Model. Journal of Biomechanics 20: 487-497.

Deng, Y.C., Li, X., Liu, Y. (1999) Modeling of the Human Cervical Spine Using Finite Element Techniques. SAE 1999-01-1310.

Deng, Y.C., Fu, J. (2002) Simulation and Identification of the Neck Muscle Activities During Head and Neck Flexion Whiplash. SAE 2002-01-0017.

De Jager, M., Sauren, A., Thunnissen, J., and Wismans, J. (1994) A Three-Dimensional Head-Neck Model: Validation for Frontal and Lateral Impacts. Stapp Car Crash Journal 38: 93-109. SAE Paper Number 942211.

De Jager, M., Sauren, A., Thunnissen, J., and Wismans, J. (1996a) A Global and a Detailed Mathematical Model for Head-neck Dynamics. Stapp Car Crash Journal 40: 269-281. SAE Paper 962430.

De Jager, M.K.J. (1996b) Mathematical Head-Neck Models for Acceleration Impacts. PhD thesis, University of Eindhoven.

Frechede, B., Saillant, G., Lavaste, F., and Skalli, W. (2003) Relationship Between Cervical Spine Curvature and Risk of Injury in the Case of Sagittal Impact: A Finite Element Analysis. 2003 International IRCOBI Conference on the Biomechanics of Impacts: 355-356.

Goldsmith, W., Deng, Y.C., and Merrill, T.H. (1984) Numerical Evaluation of the Three-Dimensional Response of a Human Head-Neck Model to Dynamic Loading. In SAE Government Industry Meeting and Exposition. SAE 840861.

Halldin, P.H., Brolin, K., Kleiven, S., Von Holst, H., Jakobsson, L., Palmertz, C. (2000) Investigation of Conditions That Affect Neck Compression-Flexion Injuries Using Numerical Techniques. Stapp Car Crash Journal 44. SAE 2000-01-SC10.

Happee, R., Morsink, P., and Wismans, J. (1999) Mathematical Human Body Modeling for Impact Loading. In Digital Human Modeling for Design and Engineering, International Conference The Hague: 1-9. SAE 1999-01-1909.

Happee, R., Ridella, S., Nayef, A., Morsink, P., de Lange, R., Bours, R., and Van Hoof, J. (2000) Mathematical Human Body Models Representing a Mid Size Male and a Small Female For Frontal, Lateral and Rearward Impact Loading. 2000 International IRCOBI Conference on the Biomechanics of Impacts.

Hayamizu, N., Miki, K., and King, A.I. (1999) Analysis of Head and Neck Response During Side Impact. In SAE International Congress and Exposition. SAE 1999-01-0717.

Huston, R.L., Huston, J.C., and Harlow, M.W. (1978a) Comprehensive, Three-Dimensional Head-Neck Model for Impact and High-Acceleration Studies. Aviation, Space, and Environmental Medicine 49: 205-210.

Huston, R.L., and Passerello, C.E. (1978b) Multibody Dynamics Including Translation Between the Bodies – With Application to Head-Neck Systems. Report Number AD-A062114.

Iwamoto, M., Kisanuki, Y., Watanabe, I., Furusu, K., Miki, K., Hasegawa, J. (2002) Development of a Finite Element Model of the Total Human Model for Safety (THUMS) and Application to Injury Reconstruction. 2002 International IRCOBI Conference on the Biomechanics of Impacts: 31-42.

Jakobsson, L., Norin, H., Jernstrom, C., Svensson, S.E., Johnsen, P., Isaksson-Hellman, I., and Svensson, M.Y. (1994) Analysis of Different Head and Neck Responses in Rear-End Car Collisions Using a New Humanlike Mathematical Model. 1994 International IRCOBI Conference on the Biomechanics of Impacts: 109-125.

Kleinberger, M. (1993) Application of Finite Element Techniques to the Study of Cervical Spine Mechanics. Stapp Car Crash Journal 37: 261-272.

Li, Y., Bishop, P.J., Wells, R.P., and McGill, S.M. (1991) A Quasi-Static Analytical Sagittal Plane Model of the Cervical Spine in Extension and Compression. Stapp Car Crash Journal 35: 419-433. SAE 912917.

Lizee, E., Robin, S., Song, E., Bertholon, N., Le Coz, J.Y., Besnault, B., and Lavaste, F. (1998) Development of a 3D Finite Element Model of the Human Body. Stapp Car Crash Journal 42: 115-138. SAE 983152.

McElhaney, J., Snyder, R.G., States, J.D., and Gabrielsen, M.A. (1979) Biomechanical Analysis of Swimming Pool Neck Injuries. Automotive Engineering Congress and Exposition. SAE 790137.

Melvin, J.W., McElhaney, J.H., and Roberts, V.L. (1972) Improved Neck Simulation for Anthropometric Dummies. Stapp Car Crash Journal 16: 45-60. SAE 720958.

Meijer, R., Parenteau, C., Van Hoof, J., and Gopal, M. (2003) Validation of a MADYMO Mathematical Human Body Model with Detailed Neck in Low Speed Lateral Impacts. 2003 International IRCOBI Conference on the Biomechanics of Impacts: 357-358.

Murakami, D., Kitagawa, Y., Kobayashi, S., Kent, R., and Crandall, J. (2004) Development and Validation of a Finite Element Model of a Vehicle Occupant. SAE 2004-01-0325.

Nightingale, R.W., Camacho, D.L., Armstrong, A.J., Robinette, J.J., and Myers, B.S. (2000) Inertial Properties and Loading Rates Affect Buckling Modes and Injury Mechanisms in the Cervical Spine. Journal of Biomechanics 33: 191-197.

Nitsche, S., Krabbel, G., Appel, H., and Haug, E. (1996) Validation of a Finite Element Model of the Human Neck. 1996 International IRCOBI Conference on the Biomechanics of Impacts: 107-122.

Paver, J.G., Khatha, T.P., Piziali, R.L., Whitestone, J., Kaleps, I., and Taylor, C. (1990) The Prediction of Hybrid III Manikin Head-Neck Kinematics and Dynamics. SAE International Congress and Exposition. SAE 900540.

Roychoudhury, R., Sun, D., Hamid, M., and Hanson, C. (2000) 5th Percentile Driver Out of Position Computer Simulation. SAE 2000 World Congress. SAE 2000-01-1006.

Ruan. J., El-Jawahri, R., Chai, L., Barbar, S., Prasad, P. (2003) Prediction and Analysis of Human Thoracic Impact Responses and Injuries in Cadaver Impacts Using a Full Human Body Finite Element Model. Stapp Car Crash Journal 47. SAE paper number 2003-22-0014.

Seemann, M.R., Lustick, L.S., and Frisch, G.D. (1984) Mechanism for Control of Head and Neck Dynamic Response. Stapp Car Crash Journal 28: 207-222. SAE 841669.

Tien, C.S., and Huston, R.L. (1985) Biodynamic Modelling of the Head/Neck System. SAE International Congress and Exposition. SAE 850438.

Tien, C.S., and Huston, R.L. (1987) Numerical Advances in Gross-Motion Simulations of Head/Neck Dynamics. Journal of Biomechanical Engineering, 109: 163-168.

Van den Kroonenberg, A., Thunnissen, J., and Wismans, J. (1997) A Human Model for Low-Severity Rear-Impacts. 1997 International IRCOBI Conference on the Biomechanics of Impacts: 117-132.

Van der Horst, M.J., Thunnissen, J.G.M., Happee, R., Van Haaster, R.M.H.P., and Wismans, J.S.H.M. (1997) The Influence of Muscle Activity on Head-Neck Response During Impact. Stapp Car Crash Journal 41: 487-507. SAE 973346.

Van der Horst, M.J., Bovendeerd, P.H.M., Happee, R., Wismans, J.S.H.W., and Kingma, H. (2001) Simulation of Rear End Impact with a Full Body Human Model with a Detailed Neck: Role of Passive Muscle Properties and Initial Seating Posture. Proc. ESV Conference 17, Amsterdam, The Netherlands. NHTSA, USA. Paper Number 119.

Van der Horst, M.J. (2002) Human Head Neck Response in Frontal, Lateral and Rear End Impact Loading: Modeling and Validation. The Netherlands: PhD dissertation, University of Eindhoven.

Van Ee, C.A., Chasse, A.L., and Myers, B.S. (2000) Quantifying Skeletal Muscle Properties in Cadaveric Test Specimens: Effects of Mechanical Loading, Postmortem Time, and Freezer Storage. Journal of Biomechanical Engineering, 122: 9-14.

Van Ee, C.A., Nightingale, R.W., Camacho, D.L.A., Chancey, V.C., Knaub, K.E., Sun, E.A., and Myers, B.S. (2000) Tensile Properties of the Human Muscular and Ligamentous Cervical Spine. Stapp Car Crash Journal 44. SAE 2000-01-SC07.

Van Hoof, J., Meijer, R., and Van der Horst, M. (2002) Effects of Muscle Activation and Seating Posture in Rear End Impact Using a Human Model with a Detailed Neck. Proc. 2002 World Congress of Biomechanics.

Weerappuli, D.P.V., Sin, D.Z., and Stanecki, P. (1998) Predicting the Response of a CART Driver in a Crash Using Mathematical Modeling. In SAE Motorsports Engineering Conference and Exposition. SAE 983069.

Williams, J.L., and Belytschko, T.B. (1983) A Three-Dimensional Model of the Human Cervical Spine for Impact Simulation. Journal of Biomechanical Engineering, 105: 321-331.

Winters, J.M. (1990a) Hill-Based Muscle Models: A Systems Engineering Perspective. Winters, J.M., and Woo, S.L.Y. Multiple Muscle Systems: Biomechanics and Movement Organization: 69-93. Springer-Verlag.

Wismans, J.S.H.M., Van den Kroonenberg, A.J., Hoofman, M.L.C., and Van der Horst, M.J. (1998) Neck Performance of Human Substitutes in Frontal Impact Direction. In NATO RTO Meeting Proceedings 20; Models for Aircrew Safety Assessment: Uses, Limitations and Requirements: 5-1-5-6. North Atlantic Treaty Organization Research and Technology Organization.

Yamazaki, K., Ono, K., and Kaneoka, K. (2000) A Simulation Analysis of Human Cervical Spine Motion During Low Speed Rear-End Impacts. SAE International Congress and Exposition. SAE 2000-01-0154.

Yang, K.H., and Le, J. (1992) Finite Element Modeling of Hybrid III Head-Neck Complex. Stapp Car Crash Journal 36: 219-233. SAE 922526.

Yang, K.Y., Zhu, F., Luan, F., Zhoa, L., and Begeman, P.C. (1998) Development of a Finite Element Model of the Human Neck. Stapp Car Crash Journal 42: 195-205. SAE 983157.

Yang, K.H., Beillas, P., Zhang, L., Lee, J.B., Shah, C., Hardy, W., Demetropoulos, C., Tashman, S., and King, A.I. (2003) Advanced Human Modeling for Injury Biomechanics Research. SAE 2003-01-2223.

Yoshida, H., and Tsutsumi, S. (2002) Finite Element Analysis Using Muscle Elements and Experimental Analysis With a New Flexible Neck Model of Whiplash Injuries in Rear-End Collisions. SAE 2002-01-0021.

Virginia Tech - Wake Forest
Center for Injury Biomechanics

www.cib.vt.edu

CIB Report Number 2006-100

Failure Properties of the Human Thoracolumbar Spine Applicable to Far-Side Automotive Impacts

PREPARED FOR

Far-Side Impact Research Group

PREPARED BY

Andrew Kemper and Stefan Duma
Virginia Tech – Wake Forest
Center for Injury Biomechanics
Department of Mechanical Engineering
Blacksburg, VA 24061
(540) 231-3945
duma@vt.edu

June 23, 2006

1. Introduction

The human spine is a complex load bearing structure that has been the focus of numerous biomechanical studies. These studies provide valuable data that can be used to characterize both vertebral bodies and intervertebral discs, validate computational models, and provide insight on the mechanisms that result in spinal injuries. The literature covers a range of both nondestructive and destructive testing of the entire spinal column, C1-L5. However, this document will focus primarily on the destructive, or failure, testing of the thoracolumbar spine, T1-L5. The literature summarized in this document provides invaluable failure data that can be used in the development of thoracolumbar spine injury tolerances for far-side automotive impacts.

2. Summary of Literature

The research aimed at determining the failure properties of the thoracolumbar spine can be broken up into three main areas: isolated vertebral bodies; functional spinal units; and multiple vertebral body spinal segments. The literature can then be further divided into different experiment types within each of these areas: compression, tension, shear, and bending (Figure 1). The remainder of this document summarizes the literature concerning the different experiment types within each of the three main areas of failure testing.

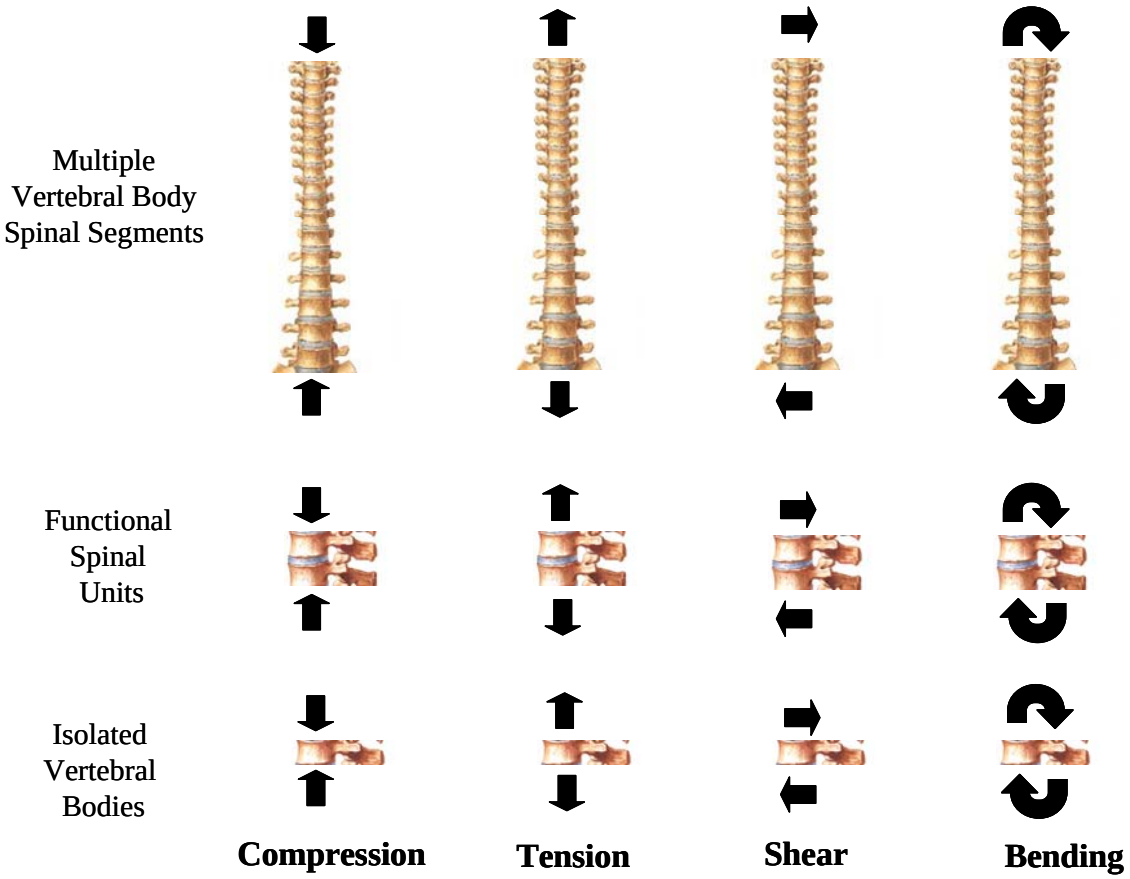

Figure 1: Various types of spinal column failure property testing.

2.1. Isolated Vertebral Bodies

Numerous researchers have investigated the failure properties of isolated vertebral bodies, which is a primary support structure in the spinal column. An isolated vertebral body is one that has been removed from the spinal column and cleaned of any soft tissue, ligaments, and intervertebral discs. The primary method of testing isolated vertebral bodies has been axial compression. Failure has been described by most researchers as crushing of the vertebral body generally accompanied by an audible crack and leaking of marrow from the body. Messerer (1880) reported the average compressive failure load for the upper thoracic vertebral bodies, middle thoracic vertebral bodies, lower thoracic vertebral bodies, and lumbar vertebral bodies to be 1957 N, 2275 N, 3560 N, and 3914 N respectively. Sonoda (1962) reported the average compressive failure load for the upper thoracic vertebral bodies, middle thoracic vertebral bodies, lower thoracic vertebral bodies, and lumbar vertebral bodies of all cadavers (20-79 yrs) to be 3028 N, 3388 N, 4493 N, and 4954 N respectively. Sonoda (1962) also reported the compressive average failure load for the upper thoracic vertebral bodies, middle thoracic vertebral bodies, lower thoracic vertebral bodies, and lumbar vertebral bodies of just the younger cadavers (20-39 yrs) to be 3630 N, 4228 N, 6317 N, and 7161 N respectively. Neither Messerer (1880) nor Sonoda (1962) reported the loading rate at which the vertebral bodies were tested. Hanssen (1979) reported the compressive average failure load for the lumbar vertebral bodies of all cadavers (31-79 yrs) and young male cadavers (31-45 yrs) to be 3834 N and 6701 N respectively. Hutton (1979) reported the compressive average failure load for the lumbar vertebral bodies of all cadavers (17-65 yrs) tested at 0.1 mm/s and 5mm/s to be 5347 N and 7215 N. Hutton (1979) reported the compressive average failure load for the lumbar vertebral bodies of just the young cadavers (17-50 yrs) tested at 0.1 mm/s and 5mm/s to be 6066 N and 7861 N respectively. Therefore, Hutton (1979) showed that the failure load of thoracic vertebral bodies in axial compression is both rate and age dependent. Pintar (1986) tested vertebral bodies at a loading rate of 2.54 mm/s, and reported the average compressive failure load for T1-T6, T7-T12, and L1-L5 to be 2642 N, 3264 N, and 4590 N respectively. Kazarian (1977) tested thoracic vertebral bodies from young cadavers (26-38 yrs) in axial compression while controlling for vertebral body level, at three different loading rates: 0.0889 mm/s, 8.89 mm/s, and 889 mm/s. Kazarian (1977) reported the average failure loads for each loading rate to be 3896 N, 5374 N, and 8691 N respectively. Like previous researchers, Kazarian (1977) also reported that for each loading rate the average failure load increased from superior to inferior vertebral bodies.

2.2. Functional Spinal Units

Functional spinal units (FSU), defined as an intervertebral disc and all or part of the two adjacent vertebral bodies, have been the most extensively studied of the three areas of spinal failure property research. The most desirable failure property of FSUs, with respect to far-side automotive impacts, is lateral bending. Unfortunately, there have been no studies that have investigated the failure properties of FSUs in lateral bending. Therefore, this section only summarizes the key studies that have investigated the failure properties of FSUs in compression, tension, and shear.

Similar to isolated vertebral bodies, the primary method of testing FSUs has been axial compression. Brown (1957) reported the compressive average failure load of lumbar FSUs to be 5204 N. Perry (1957) reported the average compressive failure load of lumbar FSUs due to static loading of all cadavers (<40 to >60 yrs) and younger cadavers (<40 yrs) to be 5284 N and 7636 N respectively. Sonoda (1962) reported the average compressive failure load for the upper thorax, middle thorax, and lumbar FSUs to be 4415 N, 11282 N, and 14715 N respectively. Neither Brown (1957) nor Sonoda (1962) reported the loading rate used for testing. Yoganandan (1989) tested thoracolumbar FSUs with both normal and degenerated discs at a loading rate of 2.54 mm/s and found the average compressive failure loads to be 11030 N and 5300 N, respectively. Duma (2006) tested lumbar FSUs at a loading rate of 1000 mm/s and found the average compressive failure load to be 12411 N. The primary modes of failure resulting from this type of testing have been reported to be fractures of the end-plate and crushing of the vertebral body. Injury to the intervertebral disc a result of a single axial compression loading event, static or dynamic, has been found to be rare.

Although axial compression has been the primary method of testing, a limited number of researchers have investigated the failure properties of FSUs in pure tension. Sonoda (1962) reported the average tensile failure loads of the upper thorax, lower thorax, and lumbar regions to be 1156 N, 2391 N, and 3185 N respectively. Pintar (1986) tested FSUs at a loading rate of 10 mm/s, and reported the average tensile failure loads of the thoracic and lumbar regions to be 597 N and 1254 N, respectively. Unfortunately, it is difficult to determine the reason for the differences in the results reported by the two researchers because Sonoda (1962) did not report the loading rate at which the specimens were tested. Sonoda (1962) and Pintar (1986) both reported that primarily failure occurred either fully or partially at the endplate junction.

There has only been one researcher to the author's knowledge that has investigated the failure properties of FSUs in direct shear. Sundararajan (2005) tested FSUs from the lumbar spine with a preload of 1000 N at two shear loading rates, and reported the average shear failure load at 0.5 mm/s and 500 mm/s to be 1850 N and 2616 N respectively. Sundararajan (2005) reported the primary failure mode at quasi-static shear forces to be disc-endplate separation accompanied by failure of posterior bony structures and the facet joint capsule. Sundararajan (2005) reported the failure mode at dynamic shear forces to be disc injuries and failure of bony fractures and the facet capsule separation. Disc injuries were not described in detail for the dynamic tests.

2.3. Multiple Vertebral Body Spinal segments

The literature on the failure properties of multiple vertebral body spinal segments of the thoracolumbar spine is the most limited of the three main areas of spinal failure property research. However, there are a few studies that provide valuable insight into the failure properties and failure mechanisms of multiple thoracolumbar vertebral body spinal segments (Yoganandan, 1988; Myklebust, 1989; Duma, 2006). The testing type, failure properties, and failure modes of these studies have been summarized (Table 1).

Similar to FSU testing, there have been no studies that have investigated the failure properties of multiple thoracolumbar vertebral body spinal segments in lateral bending. However, Demetropoulos (1988) conducted sub-failure stiffness testing on 10 multiple lumbar vertebral body spinal segments, T12-L5, in compression, tension, flexion, extension, lateral bending, anterior shear, posterior shear, and lateral shear. The average maximum sub failure moment in lateral bending was reported to be 113 Nm. The average maximum sub failure load in anterior shear, posterior shear, and lateral shear was reported to be 830 N, 1760 N, and 150 N respectively.

Table 1: Failure properties of multiple vertebral body spinal segments.

Reference	Spinal Level	Experiment	Loading Rate	Average Failure Load (N)	Average Failure Moment (N-m)	Failure Mode
Yoganandan (1988)	T3-L5 (9) T2-L5 (4) T4-L5 (1) C2-L5 (2) T6-L5 (2)	compression-flexion	2.5 mm/s	2344 1192 444 679 5418	177 99 289 84 284	Spinal column fracture due to wedging (T10-L2)
	T2-L3 T3-L2 T8-L3	Three-point Bending (flexion)	2.5 mm/s	1681 2170 1432	201 326 129	Center of spine at point of maximum flexural moment
	T12-L5 T4-L4 T10-L2	Four-point Bending (flexion)	2.5 mm/s	4893 1712 1544	245 86 77	Center of spine at point of pure flexural moment and no shear
Myklebust (1989)	T2-T9 T10-L1 (n=14)	compression (neck flexed)	ranged from 10-1200 mm/s	1223 2680	N/R	Wedge fractures from T9-L1
	intact cadaver (n=4)	Compressive load applied to T1	10 mm/s	1788	N/R	wedge /compression fractures at thoracolumbar junction
Duma (2006)	T12-L5 (n=2)	Axial compression (anatomically oriented in seated position)	1000 mm/s	5460	201	wedge /compression fractures of T12
FAA (1996)	Compressive lumbar load limit during restraint system testing POD in line with spinal column		dynamic	6672	-	N/A

3. Suggested Thoracolumbar Allowable Limits

While all is not know with respect to the failure properties of the spine and there are many methods of testing, the following provides a first order approximation for thoracolumbar injury criteria. Allowable limits for the thoracolumbar spine were developed based on the failure properties reported from all three of the areas of spinal failure property research, (Table 2). The suggested criteria was determined by averaging the failure data, rounded to the nearest hundredth, of predominantly young male cadavers tested at static to semi dynamic rates. Therefore, the suggested criteria can be used for testing with the 50th Percentile Hybrid III dummy. If there was insufficient data for certain regions in a specific testing mode, then the criteria was scaled based on the averages reported for compression testing because it was the most complete data set. Allowable limits are suggested for the upper thorax, middle thorax, and lumbar regions because these regions correspond to the locations of spinal load cells in the 50th Percentile Hybrid III dummy.

Table 2: Suggested allowable limits for the thoracolumbar spine.

	Pure Compression (N)	**Pure Tension (N)**	**Pure Shear (N)**	**Combined Compression/ Moment**
Upper Thoracic	3100	800	900	100 N-m (@ 1400 N)
Middle Thoracic	4500	1600	1300	146 N-m (@ 2000 N)
Lumbar	6200	2200	1800	200 N-m (@ 2430 N)

4. References

Brown, T., *et al* (1957). Some mechanical tests on the lumbosacral spine with particular reference to the intervertebral disks. J. Bone and Joint Surg. 39-A(5), pp: 1135-1164.

Demetropoulos, C, *et al* (1998). Mechanical properties of the cadaveric and hybrid II Lumbar spines. Proceedings of the 42nd Stapp car crash conference, SAE paper number 983160. pp: 1-10.

Duma, S, *et al* (2006). Biomechanical response of the lumbar spine in dynamic compression. biomedical sciences instrumentation symposium. 42, pp: 476-481.

Federal Aviation Administration (1996). Dynamic evaluation of seat restraint systems and occupant protection on transportation airplanes. Advisory Circular Number: 25.562-1A.

Hansson, T, *et al.* (1979). The bone mineral content and ultimate compressive strength of lumbar vertebrae. Spine 5(1), pp: 46-55.

Hutton, W, *et al* (1979). The compressive strength of lumbar vertebrae, J. Anat, 129(4), pp:753-8.

Kazarian, L and Graves, G (1977). Compressive strength characteristics of the human vertebrae centrum. Spine 2(1), pp: 1-14.

Messerer, O (1880). Uber elasticitat and festigkeit der meuschlichen knochen. Stutgrat, J.G. Cottaschen Buchhandeling.

Myklebust, J (1989). Experimental spinal trauma studies in human and monkey cadavers. Proceedings of the 27th Stapp car crash conference, SAE paper number 831614. pp: 149-161.

Perry, O (1957). Fracture of the vertebral end-plate in the lumbar spine. Acta Orthop. Scad. 25 (suppl.), pp: 2-101.

Pintar, F (1986). The biomechanics of spinal elements. Doctoral Dissertation. Marquette University Graduate School. Milwaukee, WI.

Sonoda, T (1962). Studies on the strength for compression, tension, and torsion of human vertebrae column. J. Kyoto Pref. Med. Univ. 71, pp: 659-702.

Sundararajan, S (2005). Characteristics of PMHS lumbar motion segments in lateral shear. Proceedings of the 49th Stapp car crash conference, pp: 367-379.

Yoganandan, N, *et al.* (1989). Stiffness and strain energy criteria to evaluate the threshold of injury to an intervertebral joint. J. Biomechanics 22, pp: 135-142.

Yoganandan, N, *et al.* (1988). Biomechanical investigations of the human thoracolumbar spine. SAE technical paper number 881331. pp: 1-9.

Virginia Tech - Wake Forest
Center for Injury Biomechanics
www.cib.vt.edu

CIB Report Number 2007-010

Humerus and Forearm Bending Fracture Injury Risk Functions for the 50th Percentile Male

PREPARED FOR

The Far Side Research Group
Attn: Ken Diggs and Brian Fildes

PREPARED BY

Stefan Duma, Anthony Santago, Joesph Cormier,
Narayan Yoganandan, Frank Pintar

June 14, 2007

Introduction

The purpose of this report is to develop injury risk functions for mid-shaft forearm and humerus bending fractures that are scaled to the 50th percentile male. In addition, the functions are scaled for dynamic applications such as those encountered in automobile applications. It is anticipated that these risk functions will be utilized with an instrumented upper extremity during vehicle testing.

For this study, published data was gathered from a range of experiments with male human cadaver upper extremities. Depending on the application, three separate scaling processes were utilized before the data was input for a risk function. First, the data was scaled depending on the orientation of the test or specific anthropometric considerations, such as pronation versus supination in the forearm. Second, the data was mass scaled to that of the 50th percentile male occupant (Eppinger, 1984). Third, given that some tests were performed at a quasi-static rate, the peak moments were scaled to simulate dynamic strain rates observed in cadaver upper extremity tests subjected to a deploying airbag.

Survival analysis was utilized to develop the risk functions. A Weibull model was chosen because of its increasing hazard model with severity and the closed form solution of its Cumulative Distribution Function (Lee 2003). The Weibull CDF is given by, (Equation 1), where λ and γ are the scale and shape parameters respectively and x is the measured bending moment. This function provides an estimate of risk of injury using the maximum likelihood estimate of the scale and shape parameters (Allison 1995, Cantor 2003).

$$\text{Risk of fracture} = 1 - e^{-(\lambda * x)^{\gamma}} \qquad \textit{Equation 1}$$

Forearm Fracture Risk Function

Data from a total of 28 experiments on male cadaver forearms were gathered from two primary studies (Figure 1 and Table 1) (Pintar, 1998, Duma, 2002). Since the forearm has been shown to be weaker in the pronated position, all supinated tests were scaled down by approximately 14% which was the difference between matched pair tests (Duma, 2002). Next, the moments were scaled to the 77kg average male mass. Since both sets of tests were performed dynamically at approximately the same loading rate, no rate scaling was done. The survival analysis and corresponding risk data is presented in Equation 2 and Figure 3.

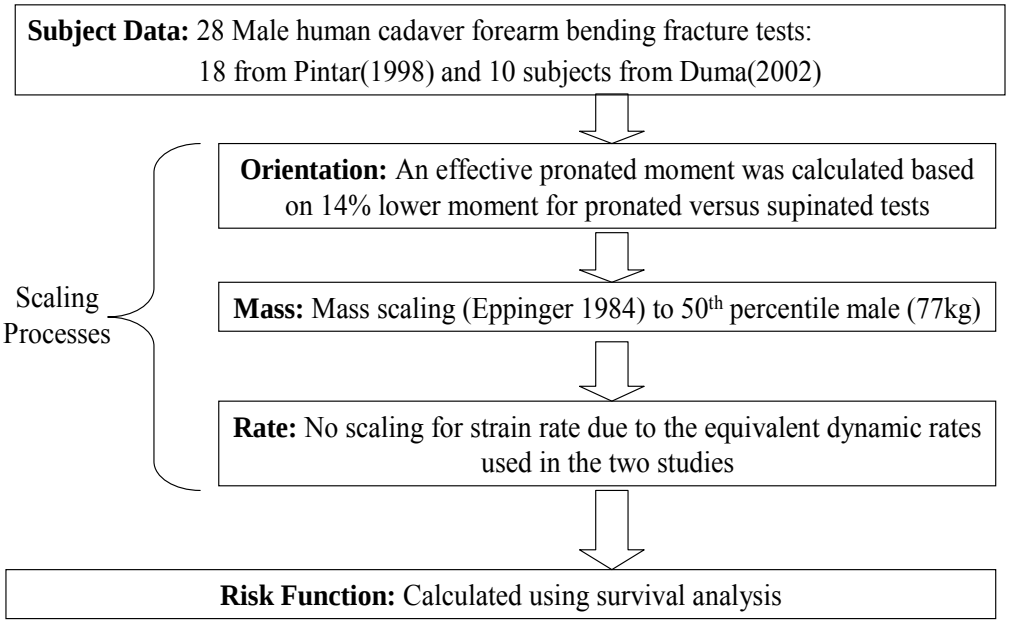

Figure 1: Outline of forearm injury risk function creation process.

$$\text{Risk of forearm fracture} = 1 - e^{-(0.0092 * x)^{4.409}} \qquad \textit{Equation 2}$$

- 25% Risk = 82Nm
- 50% Risk = 100Nm
- 75% Risk = 117Nm

Table 1: Forearm fracture data for each subject.

Paper	Test Number	Age	Body Mass	Moment	Orientation	Effective Pronated Moment	Mass Scaled Moment
		(years)	(kg)	(Nm)	Orientation	(Nm)	(Nm)
Duma 2002	1	50	63.5	116.0	supinated	100	122
Duma 2002	2	57	99.9	109.0	supinated	94	73
Duma 2002	3	48	80.3	141.0	supinated	121	117
Duma 2002	4	60	72.1	132.0	supinated	113	122
Duma 2002	5	63	70.0	132.0	supinated	113	126
Duma 2002	6	50	63.5	102.0	pronated	88	125
Duma 2002	7	57	99.9	99.0	pronated	85	77
Duma 2002	8	48	80.3	118.0	pronated	101	114
Duma 2002	9	60	72.1	114.0	pronated	98	123
Duma 2002	10	63	70.0	107.0	pronated	92	119
Pintar 1997	1	41	87.0	76.5	supinated	66	59
Pintar 1998	2	74	90.0	163.2	supinated	140	121
Pintar 1999	3	74	79.4	119.2	supinated	102	100
Pintar 2000	4	44	124.7	186.0	supinated	160	99
Pintar 2001	5	72	68.0	48.3	supinated	41	47
Pintar 2002	6	41	90.0	130.0	supinated	112	96
Pintar 2003	7	69	79.4	142.5	supinated	122	120
Pintar 2004	8	66	68.0	87.1	supinated	75	85
Pintar 2005	9	66	124.7	178.9	supinated	153	96
Pintar 2006	10	72	87.0	142.1	supinated	122	109
Pintar 2007	11	69	81.6	101.7	supinated	87	83
Pintar 2008	12	68	70.3	76.0	supinated	65	72
Pintar 2009	13	78	47.6	112.5	supinated	97	158
Pintar 2010	14	44	97.5	99.0	supinated	85	68
Pintar 2011	15	68	81.6	101.4	supinated	87	83
Pintar 2012	16	78	70.3	68.6	supinated	59	65
Pintar 2013	17	61	47.6	78.3	supinated	67	110
Pintar 2014	18	61	97.5	118.6	supinated	102	81

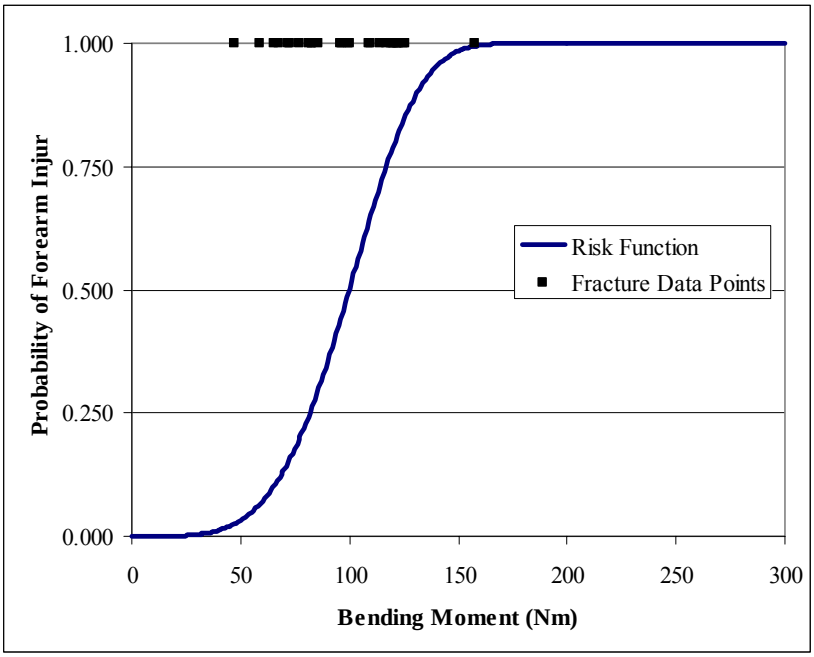

Figure 2: Forearm fracture risk function for the 50th percentile male.

Humerus Fracture Risk Function

Data from a total of 25 experiments on male cadaver humeri were gathered from two primary studies (Figure 3 and Table 2) (Kirkish, 1996; Kallieris, 1997). Given the symmetry of the humerus, all bending orientations were considered equal. Moreover, Kirkish (1996) found this to be statistically correct. Next, the moments were scaled to the 77kg average male mass. Given the widly varing impact rates between the tests, the moments were scaled to the equivalent 3.7 strains/second loading rate which was found from cadaver tests with side airbag impacts to the humerus. A limit was placed on this scaling in that everything below 0.005 m/s was treated as 0.005 m/s. While bone is stronger the faster you load it, this relationship reaches a limit. In other words, if you test at an infinitely slow rate, the bone is not infinitely weaker. Finally, the survival analysis and corresponding risk data is presented in Equation 3 and Figure 4.

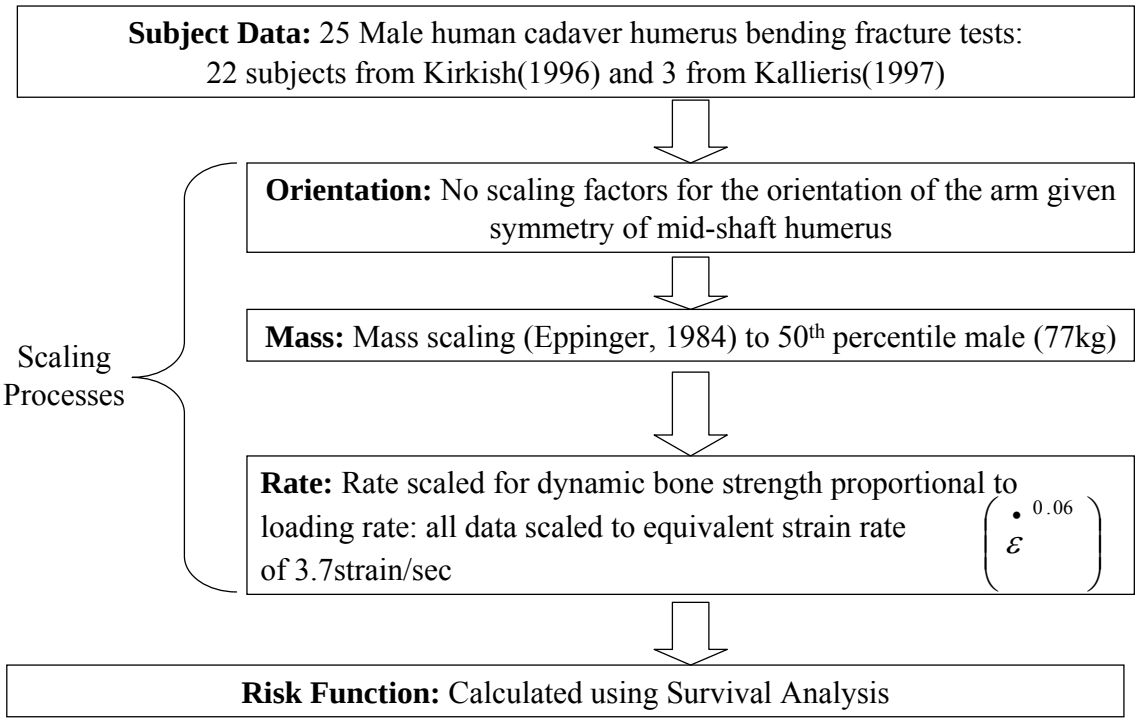

Figure 3: Outline of humerus injury risk function creation process.

$$\text{Risk of humerus fracture} = 1 - e^{-(0.0036 * x)^{4.871}} \qquad \textit{Equation 3}$$

- 25% Risk = 214Nm
- 50% Risk = 257Nm
- 75% Risk = 296Nm

Table 2: Humerus fracture data for each subject.

Paper	Test	Age	Body Mass	Orginial moment	Test Rate	Mass Scaled Moment	Rate Scaled moment
		(years)	(kg)	(Nm)	m/s	(Nm)	(Nm)
Kirkish 1996	1	66	55.3	149	0.218000	209	248
Kirkish 1996	2	66	55.3	182	0.002500	256	380
Kirkish 1996	3	59	58.5	106	0.000635	141	209
Kirkish 1996	4	59	58.5	118	0.218000	157	186
Kirkish 1996	5	67	65.3	102	0.000635	121	180
Kirkish 1996	6	69	86.6	240	0.000635	215	320
Kirkish 1996	7	69	86.6	247	0.218000	222	262
Kirkish 1996	8	61	75.7	151	0.218000	155	183
Kirkish 1996	9	61	75.7	104	0.000635	107	158
Kirkish 1996	10	75	78.9	123	0.000635	121	180
Kirkish 1996	11	75	78.9	145	0.218000	143	169
Kirkish 1996	12	66	56.2	150	0.218000	207	246
Kirkish 1996	13	66	56.2	151	0.000635	209	310
Kirkish 1996	15	45	81.6	190	0.000635	181	269
Kirkish 1996	16	61	59.4	110	0.000635	144	214
Kirkish 1996	17	61	59.4	148	0.218000	194	229
Kirkish 1996	18	61	53.5	150	0.000635	218	323
Kirkish 1996	19	48	56.2	187	0.218000	259	306
Kirkish 1996	20	59	47.2	133	0.000635	219	325
Kirkish 1996	21	59	47.2	160	0.218000	263	312
Kirkish 1996	22	50	79.4	216	0.218000	211	250
Kirkish 1996	23	50	79.4	211	0.218000	206	244
Kallieris 1997	C3	69	56.0	148	0.000250	205	305
Kallieris 1997	C4	86	60.0	135	0.000250	175	260
Kallieris 1997	C5	45	55.0	130	0.000250	184	273

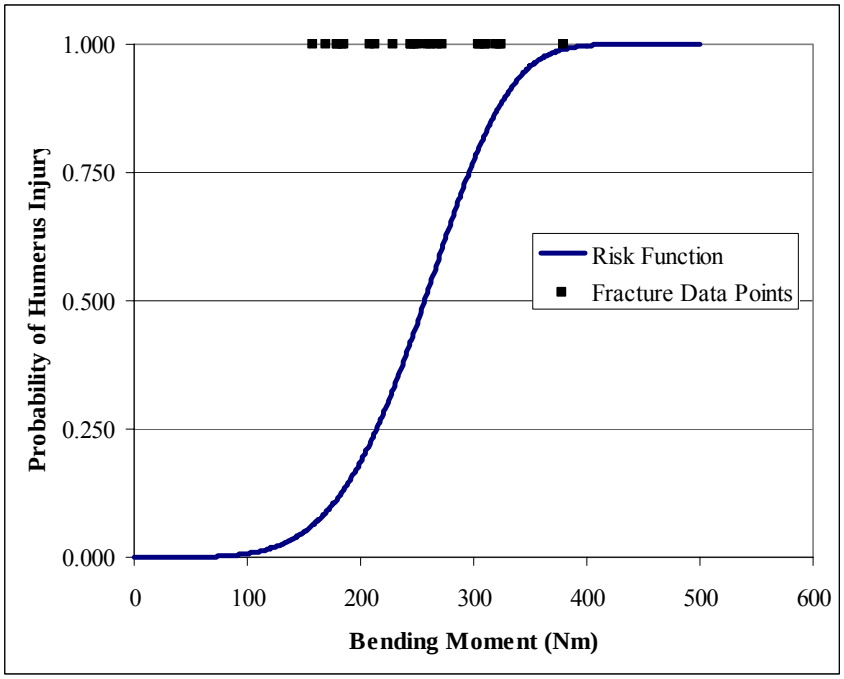

Figure 4: Humerus fracture risk function for the 50th percentile male.

References

Allison, P.D., 1995. Survival Analysis Using SAS: A Practical Guide. SAS Press, North Carolina.

Cantor, A.B., 2003. Survival Analysis Techniques for Medical Research 2nd. SAS Press, Cary NC.

Lee, E.T., Wang, J.W., 2003. Statistical Methods for Survival Data Analysis 3rd. John Wiley, New Jersey.

Eppinger, R.H., Marcus, J.H., Morgan, R.M., 1984. Development of Dummy and Injury Index for NHTSA's Thoracic Side Impact Protection Research Program. SAE paper 840885. Society of Engineers, Warrendale, PA.

Duma, S.M., et al, 2002. Fracture tolerance of the male forearm: the effect of pronation versus supination. Proc Instn Mech Engrs Vol 216 Part D: Journal of Automobile Engineering

Kirish S.L., Begeman P.C., Paravasthu N.S., 1996. Proposed Provisional Reference Values for the Humerus for Evaluation of Injury Potential. Paper number 962416. Society of Automotive Engineering, Warrendale, PA.

Pintar, F.A., Yoganandan, N., Eppinger, R.H., 1998. Response and tolerance of the human forearm to impact loading. SAE paper 983149. 42nd Stapp International Car Crash Conference, Temple, Arizona.

Kallieris, D., et al, 1997. Response and Vulnerability of the Upper Arm Through Side Airbag Deployment. Proc. 41st Stapp Car Crash Conference, pp. 101-100. Society of Automotive Engineers, Warrendale PA.

AN EXPERIMENTAL AND COMPUTATIONAL STUDY OF BLUNT CAROTID ARTERY INJURY

F. Scott Gayzik[1,2], Ola Bostrom[3], Per Örtenwall[4], Stefan M. Duma[2], Joel D. Stitzel[1,2]

[1] Wake Forest University School of Medicine, Medical Center Blvd, Winston-Salem, NC 27157
[2] Virginia Tech – Wake Forest University Center for Injury Biomechanics, Medical Center Blvd, Winston-Salem, NC 27157
[3]Autoliv Research, 447 83 Vargarda, Sweden
[4]Sahlgrenska University Hospital, Gothenburg, Sweden

ABSTRACT

A carotid artery dissection begins as a tear or defect of the intimal lining of the artery, and can lead to luminal occlusion and ultimately cerebral ischemia. Our aim is to conduct an organ level validation of a finite element model of the carotid artery using an experiment designed to elicit internal layer failure within fluid-filled carotid artery samples. A 2.4-kg beveled guillotine is dropped from three heights (0.3, 0.5 and 0.7 m) onto fluid-filled porcine carotid arteries and resulting damage is recorded. These events are modeled using finite element analysis. Stress, strain and strain rate are correlated to experimental outcome. Internal layer damage is reported in half of the experiments, with damage occurring with 100% frequency at a drop height of 0.7 m. Simulations of this experiment result in maximum principal stress and strain values of 1.43 MPa and 46.2% respectively. The strain level predicted by the model for this impact scenario approaches the strain to intimal failure level for porcine arteries found in the literature. The results of this study represent an important step in validating this finite element carotid artery model at the organ level.

Through the collective efforts of clinicians, automotive safety researchers and legislators the rate of motor vehicle traffic-related injuries per 100 million vehicle miles traveled continues to drop (NHTSA 2003). Computational modeling continues to play an important role in engineering safety interventions. Recent research has focused on modeling injuries to specific soft tissue organs in the body including the brain (Zhang, Yang et al. 2001; Takhounts, Eppinger et al. 2003), lung (Stitzel, Gayzik et al. 2005), aorta (Shah,

Yang et al. 2001; Richens, Field et al. 2004), eye (Stitzel, Duma et al. 2002) and abdomen (Lee and Yang 2001).

Blunt or penetrating carotid artery injures are commonly encountered in automobile crashes (Stemper, Stineman et al. 2005; Stemper, Yoganandan et al. 2005). The associated mortality and long term neurological morbidity of this injury are estimated at 40% and 40-80% respectively (Stemper, Yoganandan et al. 2005). Among fundamental mechanisms of blunt carotid injury that have been identified, three constitute injury patterns associated with car crash; direct blow to the neck (e.g. seatbelt), hyperextension and contralateral rotation of the neck, and basilar skull fracture (Crissey and Bernstein 1974).

On a local level, Sinson et al. postulate that the main mechanism of injury is stretching of the artery secondary to neck extension (Sinson, Yoganandan et al. 2003). Others postulate direct blunt trauma to the neck is the mechanism for the injury. Rozycki et al., in a prospective study including 797 patients, found 16% sustained belt marks and of that 16%, 3% had sustained carotid artery injury. The study implicated belt loading as a direct cause of the cerebrovascular injuries (Rozycki, Tremblay et al. 2002). A similar conclusion was reached in a post-mortem case study of blunt carotid injury (Reddy, Furer et al. 1990). In summary, both blunt trauma (pinching) or distraction (tension) are likely causes of arterial injury.

The true incidence of this injury is unknown since many victims are not screened for injury, but blunt cerebrovascular injury (BCVI) is estimated to be present in roughly 1% of trauma admissions. By comparing two successive studies of this injury Miller et al. found that the incidence of BCVIs increased with aggressive screening (Miller, Fabian et al. 2001) (Miller, Fabian et al. 2002). Other studies identified similar trends, suggesting that BCVI has been historically under diagnosed (Biffl, Moore et al. 1998; Biffl, Moore et al. 2001).

The pathophysiology of BCVI begins as an intimal disruption. Such a disruption can ultimately lead to luminal narrowing via a number of different pathways including platelet aggregation, dissection of the intimal layer of the artery, aneurysm between interstitial layers, and intramural hematoma following hemorrhage of the vasa-vasorum (Biffl, Moore et al. 2001) (Schievink 2001; Haneline and Lewkovich 2005) (Haneline and Lewkovich 2005). Internal carotid artery dissection (ICAD) is 3 to 5 times as likely to occur as vertebral artery dissection, and more than 7000 cases of internal artery dissection per year occur in the United States alone (Schievink, Mokri et al. 1994; Haneline, Croft et al. 2003). A review of the available literature found that nearly 30% of all ICAD cases are attributed to some form of trauma (Haneline and Lewkovich 2005).

The internal branch of the left and right common carotid arteries, along with the vertebral arteries together are responsible for delivering 100% of the blood supplied to the brain. Disruptions in this blood supply lead to neurological deficit with devastating consequences. With a link between automobile crash and carotid artery injury (CAI) established, understanding the complex biomechanics of the carotid artery is critical to developing improved countermeasures.

Relative to the large body of work in the literature on modeling arteries at physiologic strain rates, there are few computational studies of their behavior during dynamic impact events. Several finite element analysis (FEA) studies have been published on traumatic aortic rupture (Shah, Yang et al. 2001; Richens, Field et al. 2004), however the authors are unaware of any study investigating traumatic injury mechanics of the carotid artery using FEA. The use of finite elements is a good approach for investigating high-rate arterial injury mechanisms since internal stress and strain values can be calculated provided that the model is sufficiently validated. Additionally, the finite element method is capable of modeling the complex morphology of structures like the carotid artery (Gayzik, Tan et al. 2006).

The philosophy the authors employ in developing the FE carotid artery model consists of validation at the tissue, organ and regional level. Tissue level validation consists of modeling a simple mechanical loading condition applied to a uniform sample (e.g. a uniaxial tension test). Validity of a material model is gained by comparing the results of a tissue level model to empirical uniaxial tension data. Following tissue level validation, modeling is conducted at the organ level. The purpose of organ level validation is to apply the material model developed at the tissue level to an isolated structure composed of that material undergoing a dynamic event. Upon completion of organ level validation, sufficient confidence in the model's ability to predict the mechanical behavior of the structure under study has been compiled such that the model can be implemented at a regional level.

Data on the failure mechanics of the porcine descending aorta (PDA) at quasi-static rates (Stemper, Stineman et al. 2005) were used for tissue level validation of this carotid artery model prior to commencement of this study. Simulated engineering stress vs. strain was highly correlated ($R^2 = 0.99$) with the experimental data. Our current aim is to use the FEA results to perform organ-level validation of the carotid artery model for later use in a regional level model of the neck.

This study has an experimental and computational component. In the experiment, excised porcine carotid arteries are struck with a semicircular (5 mm-radius) edged guillotine from three

drop heights. The purpose of this experiment is to expose intact carotid arteries to sufficient axial tension and "pinching" to elicit internal layer failure. The internal layer of the carotid arteries is assessed post-impact and coded as either injured or uninjured. Simulations of the guillotine experiments are then conducted using FEA and stress, strain and strain rate associated with this dynamic impact are calculated. Stress and strain values associated with internal layer failure found in the literature are used to compare the results of the FEA and the experiment, thereby assessing the organ-level validity of the model.

CERVICAL ARTERY ANATOMY

The portions of the left and right common carotid arteries traversing the neck (cervical portions) are anatomically identical. Cervical portions are subject to higher rates of injury than thoracic and cranial portions (Schievink 2001). At the level of C4, the artery bifurcates into the internal and external carotid arteries. The internal carotid artery (ICA) supplies blood to the brain, eye, nose and forehead.

The left and right vertebral arteries also traverse the neck superiorly. These arteries pass through the transverse foramina of the cervical vertebrae. While this may increase the risk of vertebral artery injury in the case of cervical vertebrae fractures or basilar skull fractures, this passage provides additional protection against blunt trauma not present for the carotid artery, which is surrounded by soft tissue rather than bone (Miller, Fabian et al. 2002). For this reason the analysis focuses on the carotid artery, although the structure of the arteries is similar.

The arteries are composed of three laminate layers, the intima, medial and adventitia. The intima lines the lumen of the artery and consists of endothelial cells and basal lamina. The thickness of this layer is roughly 80nm, although its composition and thickness will vary depending on the size of the vessel (Fung 1993). The media is composed of smooth muscle cells and various bundles of collagenous and elastic fibrils. The adventitia contains collagen fibers, basal lamina, blood vessels and nerves. Research on healthy, aged human external iliac arteries found that the ratio of the intimal-medial thickness to the adventitial thickness is on average 1:2 (Shulze-Bauer, et al. 2003). In the present study, arterial layers were not modeled individually, an approach used in prior vessel modeling (Shah, Yang et al. 2001).

METHODS

PART I: DYNAMIC IMPACT TESTS - Young porcine carotid arteries (aged 6 months or less) were harvested from an abattoir, and tested within 24 hours of acquisition. Vessels were

stored in a physiologic salt solution (0.9%). Immediately before testing the vessel was cut to size (mean axial length, 36 mm) and one end was tied shut. The other end was fixed to a cannula which filled the lumen to atmospheric pressure only. Filled arteries were placed in a semicircular notch within a polyethylene foam encasement. The notch was sized to accommodate the filled arteries snugly (mean filled diameter of the arteries was 5.1 ± 0.6 mm), and was sufficiently lubricated to reduce friction between the foam and the artery. The foam encasement above and below the artery was flat to ensure even contact as the foam was compressed by the indenter. The foam layers above and below the carotid artery were 14 mm and 25 mm thick respectively. Clear polycarbonate was placed flush to the encasement. The initial experimental protocol called for fixed end conditions, but no tension was observed during preliminary testing so free end conditions were used for all tests. Video of the impacting event was recorded at 1000 frames/sec. Arteries were tested once and a fresh sample was used for each test.

A 2.4-kg steel indenter, with 5 mm rounded tip at the impacting edge, was mounted on a vertically sliding guillotine and used to strike the samples. The indenter was released from three heights, striking the foam-encased artery perpendicularly at its midpoint. The drop heights of 0.3, 0.5 and 0.7 m above the sample resulted in impact speeds of 2.4, 3.1, and 3.7 m/s respectively. Two samples were tested at 0.3 m, and four were tested at the remaining two drop heights for a total of 10 tests. Figure 2 in the Results section shows a progression of the 0.5 m impact.

The carotid samples were subsequently removed from the foam encasement, cut along the longitudinal axis, and fixed in formalin. Internal layer integrity was assessed by visibly inspecting the lumen of the artery for fissures or tearing and outcome was coded as either damaged or undamaged. Histological analysis was not undertaken for reasons described in the Discussion. A post-impact prepared specimen is shown in Figure 3 of the results section. The experiment was conducted at Autoliv, and only samples from postmortem animals from an abattoir were used. No experimentation was conducted at Wake Forest University Baptist Medical Center and therefore no approval was sought at the medical center.

PART II: FINITE ELEMENT MODEL OF IMPACT - The finite element model was constructed from video of the experiment and is shown in Figure 1. The video of the experiment was split into an image stack where each frame of the video was a separate file (.tif). A frame prior to the impact was used to take vessel diameter and length measurements. Calibrated tape (1 cm increments) and a ruler were clearly visible in the frame enabling accurate calibration of measurements. Four diameter measurements were taken at discrete locations along the axis of the vessel and averaged. A single

measurement was taken to determine vessel length. Because vessel geometry varied little between tests, a single video was used to construct the model. The diameter and length used in the model were 4.5 mm and 30 mm respectively. The vessel diameter used in the model is within one standard deviation of the mean diameter calculated from analysis of five video files. The vessel length was slightly less than the mean axial length. However since all vessel damage observed in the experiment occurred directly below the indenter, vessel length was considered less critical than diameter. The reasonable assumption of circular cross section was made in creating the model.

To reduce computation time, two foam blocks were modeled instead of a single foam encasement with a semi-circular notch as was used in the experiment. Foam was modeled with 8-node hexahedral elements. The mesh of the top foam was tailored to accommodate large compressive strains. The indenter and the artery were constructed of quadrilateral shell elements. Vessel shell thickness was 0.5 mm. Meshing was accomplished using Finite Element Model Builder (FEMB, Livermore Software Technology Company, Livermore, CA). Lagrangian element formulations were used for all solid structures. A hexahedral Eulerian mesh surrounds the carotid artery and lower foam section to model the movement of the fluid within the carotid artery. The total number of elements in the model is 28196. The dynamic impact was analyzed using LS-Dyna (LSTC, Livermore, CA).

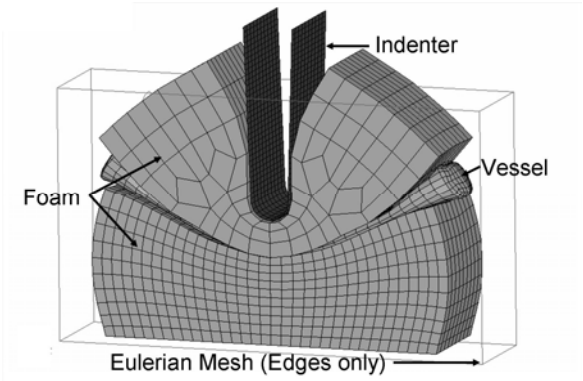

Figure 1. Finite element model of the dynamic porcine carotid tests, showing foam encasement, artery, indenter and boundary of the Eulerian flow field.

The foam was modeled using '*MAT_LOW_DENSITY_-FOAM' (*MAT_057). This foam is typically used in modeling seat cushions and side impact dummies (LSTC 2003). This model employs a user-provided stress-strain curve. The loading curve is used in the compressive regime to interpolate stresses from a calculated stretch. In the tensile regime the modulus of elasticity is used. The loading curve is nonlinear and taken the literature (Mills

and Masso-Moreu 2005). The Mills and Masso-Moreu stress vs. strain data result from drop testing of the same foam used in the present experiment. The material safety data sheet (MSDS) for the polyethylene foam provided nominal stress vs. strain data but only up to 50% compression. The literature data compared closely the MSDS data but extended out to full compression (99%). The modulus of elasticity was estimated from the slope of the compressive data.

The material model used for the carotid artery was *MAT_Simplified_Rubber (*Mat_181), a simplified model for modeling rubber-like materials under dynamic loading. The model is considered "simplified" because rather than providing coefficients for the underlying hyperelastic model (Ogden Model), the functional is computed for the uniaxial data provided (Du Bois 2003; Kolling, Du Bois et al. 2005). Uniaxial data is provided to the model in the form of stretch ratio (deformed length/undeformed length) and tensile force. Force deflection data from a quasi-static tensile test of young porcine descending aorta was used in the model (Stemper, Yoganandan et al. 2005).

The generalized form of the partial derivative of Ogden's hyperelastic strain energy density functional, with respect to the principal stretches λ is shown in Equation 1. In this equation, K is the bulk modulus, J is the volume ratio (V/V_o), λ^* is the modified stretch ratio ($\lambda^* = \lambda J^{1/3}$) and $f(\lambda)$ is a generalized function of Ogden coefficients. The simplified rubber model assumes a different form of $f(\lambda)$ than the conventional polynomial form (LSTC 2003). The alternative form of $f(\lambda)$ is shown in Equation 2. In this form, the uniaxial stress and strain data provided is used to directly calculate the function. Strain is calculated from the stretch ratio provided by the user via Equation (3) and the corresponding force is read from the uniaxial data. Stress is calculated by dividing the force by the undeformed specimen cross-sectional area.

$$\sigma_i = \frac{1}{J}\left(f(\lambda_i) - \frac{1}{3}\sum_{k=1}^{3} f(\lambda_i) \right) + K\frac{J-1}{J} \qquad (1)$$

$$f(\lambda_i) = \lambda_i \sigma_o(\varepsilon_{oi}) + \sum_{n=1}^{\infty} \lambda^{(1/2)^n} \sigma_o(\lambda^{(1/2)^n} - 1) \qquad (2)$$

$$\varepsilon_{oi} = \lambda_i - 1 \qquad (3)$$

The density of the carotid was taken as that of water. Bulk modulus was found in the literature (Duck 1991). Shear modulus was estimated from bulk modulus by assuming the carotid is nearly incompressible (Poisson's ratio of 0.499). A summary of the parameters used in the foam and carotid artery models is given in Table 1. The indenter was modeled as a rigid body.

Table 1. Parameters used in simplified rubber model of carotid artery

Porcine Carotid Artery	
Model	Simplified Rubber
Density, [g/mm^3]	1.00×10^{-3}
Bulk Modulus, [N/mm^2]	$2.71 \times 10^{+3}$
Shear Modulus, [N/mm^2]	5.20
Polyethylene Foam	
Model	Low Density Foam
Density, [g/mm^3]	36.0×10^{-6}
Elastic Modulus, [N/mm^2]	2.36×10^{-1}

Boundary conditions were set to mimic the experiment. The bottom most nodes of the foam were locked. Nodes on the edges of the foam were locked in-plane to mimic the presence of the polycarbonate sheet shown in Figure 2. The action of the simulation was modeled via a prescribed motion boundary condition applied to the indenter. The position of the indenter with respect to time was tracked for each drop height by importing the image stack created from video of the experiment into ImageJ (National Institutes of Health, http://rsb.info.nih.gov/ij/). Separate trajectories were applied as prescribed motion boundary conditions of the rigid indenter for a total of three simulations. Contact between Lagrangian solids was modeled using *Contact_Automatic_Single_Surface. Checks for initial nodal penetration from one part to a neighboring part were negative. Changes in shell thickness were included in the contact algorithm calculation. Stiffness type hourglass control was employed. Since little friction was observed in the experiment, friction between the foam and the vessel was not included.

Two procedures were conducted to give confidence to the results of the foam model; validation of the initial indenter velocity, and validation of the gross foam compression. The frame rate of 1000Hz was adequate to track the location of the indenter. Since the drop height of the indenter was carefully controlled in each case, the initial velocity was known via $v = \sqrt{(2*g*h)}$. By taking the derivative of the displacement history of the indenter a direct comparison was made to validate the initial velocity of the indenter. The second foam validation procedure was to compare the displacement of the lower foam surface of the simulation to that of the experiment. Simulated foam displacement was acquired by tracking the displacement of a node on the upper surface of the lower foam block. Displacements of the same point in the experiment were taken from video of the impacting event.

RESULTS

PART I: DYNAMIC IMPACT TESTS – Still frames from video of the impacting event are shown in Figure 2. Table 2 summarizes the results of the drop tests. Damage to the inside layer of the artery was assessed with the unaided eye, and was visible as a

distinct fissure on the lumen of the artery (Figure 3). In all tests where damage was present, the lesion occurred as a split with its long axis in the circumferential direction of the lumen and directly below the indenter. The intimal side of the artery was extremely delicate, and a lesion could be induced by simply pinching the artery. The incidence of injury increased with drop height, with 100% incidence of injury at 0.7 m. No damage was observed at 0.3 m.

Table 2. Summary drop test results

Height (m)	Number of tests	Penetration depth (mm)	Impact Speed (m/s)	Injury frequency
0.3	2	34	2.4	0%
0.5	4	36	3.1	25%
0.7	4	38	3.7	100%

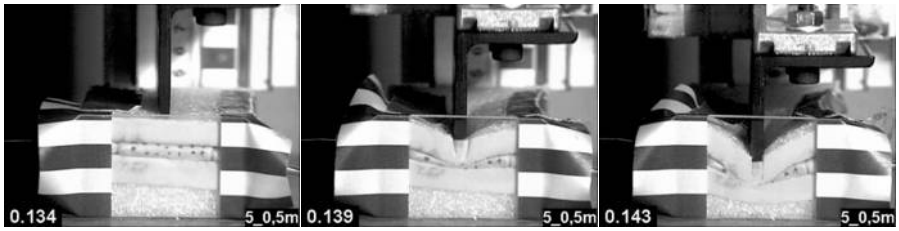

Figure 2. Stills from video of 0.5m impact showing porcine carotid artery encased in polyethylene foam and progression of indenter.

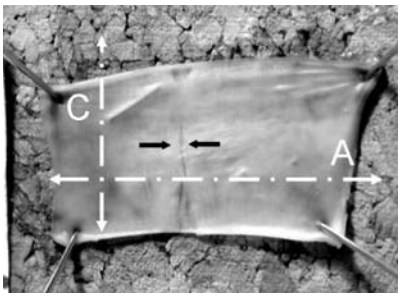

Figure 3. Post impact porcine carotid artery specimen with visible intimal damage (located by the black arrows). Circumferential and axial axes are also shown.

PART II: FINITE ELEMENT MODEL OF IMPACT – Despite some instability on initial runs the model performance was robust. Model instability was remedied by increasing the stiffness of the foam at very large strains (99.9%) and tailoring the mesh of the upper foam layer to accommodate large strains, Figure 1. A mesh convergence study was performed on the 0.7 m drop simulation wherein each element was split into either 4 or 8 elements (depending on whether the element was shell or brick). Peak stress and strain values resulting from the simulation were within 1% of the nominal mesh values. The hourglass energy in the vessel was low, (hourglass energy/internal energy ~ 2%) however was higher in the foam (ratio increased to 25%). More on the model numerical performance can be found in the discussion.

The foam validation procedures yielded positive results. The discrepancy between prescribed initial penetration velocity and calculated initial penetration velocity was less than 3% for all models. The lower foam displacement validation yielded high correlation for the 0.5 and 0.7 m drop simulations. The error between simulated and experimentally observed foam compression at max indenter penetration was less than 2% for both simulations. The 0.3 m simulation resulted in an error at max indenter penetration of 13%. Validation study results are summarized in Table 3 and Figure 4.

Table 3. Initial velocity validation data

Drop Height	Initial velocity (calculated)	Initial velocity (video)
0.3 m	2.42 m/s	2.51 m/s
0.5 m	3.13 m/s	3.13 m/s
0.7 m	3.70 m/s	3.69 m/s

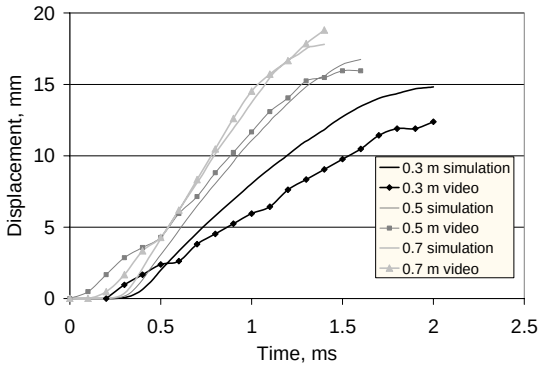

Figure 4. Results of the foam motion validation procedure. Experimental data are the location of the upper-edge the foam beneath the indenter. Simulation data are the location of the corresponding node.

Three regions of interest were defined to analyze the results of the finite element simulations (Figure 5). The top region contained 20 elements, 10 on either side of the vessel midline facing the upper foam, the bottom region mirrors the top region but faces the lower foam, and the side region contained a total of 24 elements (12 on each side). When summed, the surface area of the regions of interest covers a circumferential band about the vessel midline. Stress and strain within each region of interest were relatively uniform. Analysis of the impact event was performed by averaging the stress, strain and strain rate from each of these regions for each impact. All data was filtered using the built-in SAE filter in the post-processing software LS-PrePost (LSTC, Livermore, CA) and a cutoff frequency of 2000 Hz. Stress and strain values presented below are maximum principal stress and strain values (true stress and strain).

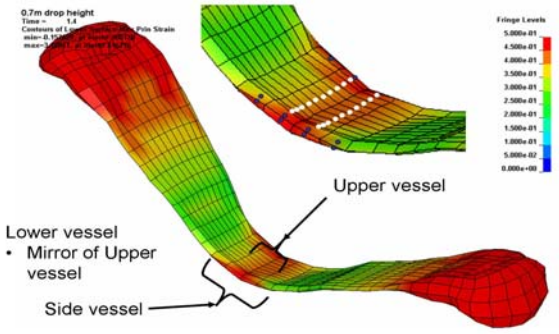

Figure 5. Regions of interest of the vessel. The upper vessel elements are denoted by white dots. The side region comprises two sets of elements denoted by dark dots, not all shown. No elements on the lower side of the vessel are visible, but they mirror the upper region.

In general, the stress and strain values occurring in the top and bottom regions were of greater magnitude than those occurring in the side region. For this reason, the analysis concentrates on the former two regions. The largest strains and strain rates occurred in the top region of the vessel. The same can not be said of the stresses, as the peak stresses were highest in the bottom region for the 0.5 and 0.7 m simulations. The difference between peak values in the top and bottom regions is within 10% in all cases, meaning the loading below the indenter was fairly uniform. Figure 6 shows the top side strain and stress resulting from each of the drop heights. A peak strain of 46% occurs in the 0.7 m simulation. This represents a 16% increase over the peak strain in the 0.3 m drop simulation. Strain rate values are fairly uniform. In the first 5 ms of the event, an average strain of 36% is achieved for all drop heights, correlating to an average strain rate of 73 strain•sec^{-1} ± 8.5 strain•sec^{-1}. Stress values increased more dramatically between drop heights than strain values. The peak stress on the section of the artery below the indenter increased 50% between the 0.3 m and 0.7 m drop, compared to an increase in stress of only 13.6% between the 0.3 m and 0.5 m drop. A summary of the strain, strain rate and stress from the simulations is provided in Table 4.

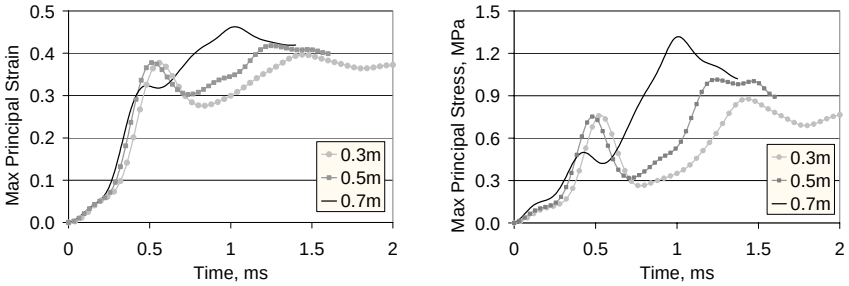

A. B.

Figure 6. Results from computational study. (A) First principal strain from top region for the three drop heights. (B) First principal stress from the same region for each drop height.

Table 4. Summary of strain, strain rate and stress values in drop simulations by region.

Height (m)	Vessel Region	5ms Strain rate (strain•sec-1)	Peak strain (%)	Peak stress (MPa)	Injury frequency (%)
0.3	Top	67.4	39.7	0.88	0
	Bottom	63.7	36.0	0.84	
0.5	Top	73.8	41.8	1.01	25
	Bottom	74.5	38.7	1.12	
0.7	Top	87.7	46.2	1.32	100
	Bottom	67.9	43.4	1.43	

A constraint placed on the Eulerian fluid bounded by the vessel ensured that the fluid remained inside the artery for the duration of the simulation. The models were investigated to verify that this constraint was obeyed throughout the simulation. Figure 7 shows plots of the fluid density for each of the three drop heights at the point of maximum indentation. The fluid density was $1 \cdot 10^{-3}$ g•m^{-3}. Volume occupied by the fluid appears dark. Fringe levels are apparent as fluid approaches the edges of the Eulerian mesh. The images show that the fluid-in-solid constraint was maintained throughout the simulation. Fluid separation is noted at the maximum intrusion of the indenter in the 0.7 m simulation (Figure 7c).

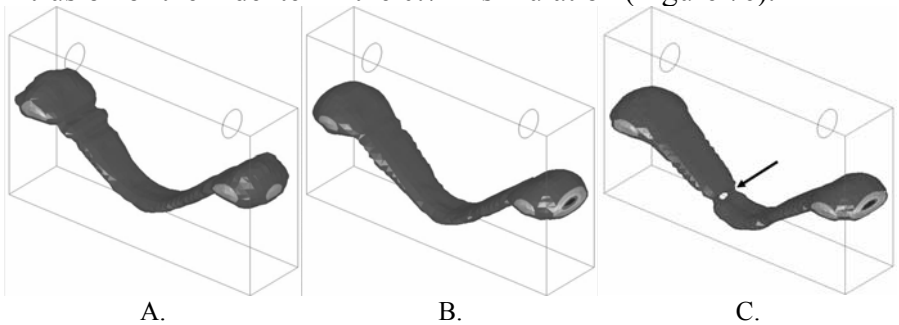

A. B. C.

Figure 7. Location of fluid within the carotid at point of furthest indentation. (A) 0.3m drop, 34 mm penetration; (B) 0.5 m drop, 36 mm penetration; (C) 0.7 m drop, 38 mm penetration. Arrow indicates location of fluid separation

This separation suggests that intima to intima contact is present at this drop height; however the lack of this phenomenon does not preclude top to bottom intimal contact. Figure 8 shows the relative distance between nodes at the upper-most and lower-most locations of the carotid artery. These nodes are precisely in the center of the model. The difference in their location gives an estimate of the distance between the upper and lower intimal layers. For all simulations the distance between nodes becomes progressively smaller as the indenter penetrates through the foam. Ultimately the distances cease to decrease, indicating that the upper and lower portions of the vessel are moving together and are in contact. The mean final separation value of the two sides of the vessel is 0.34 mm. Given the thickness of the shell (0.5 mm) it follows that the distance from the Gauss point of one shell to the closest Gauss point of an abutting but non-penetrating shell would be 0.211 mm. Therefore the final separation distance is slightly greater than the distance between Gauss points. This is not surprising since the location of the Gauss points do not coincide with the location of the nodes, and the final separation distance is a measure of nodal distance.

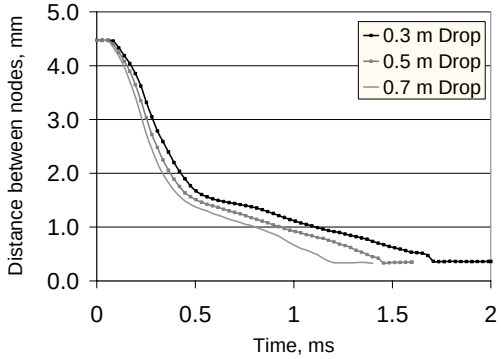

Figure 8. Distance between nodes at upper-most and lower-most points on the carotid artery at the midpoint.

DISCUSSION

The purpose of this study was to perform an organ level validation of a finite element model of the carotid artery for later use in a regional level model of the neck. This organ level validation study follows validation of the material model used for the carotid artery at the tissue level. The simulations show that all the mechanical values of interest increase between the 0.3 m and 0.7 m drops. Peak strain shows the lowest increase (16%) while the increase in peak stress is much greater.

The data used in development of the carotid artery model is the result of a study by Stemper, et al. characterizing the failure mechanics of the internal layer of the human carotid artery and

porcine descending aorta (PDA) (Stemper, Stineman et al. 2005). The authors of the latter study cut arterial samples into classic hourglass shaped mechanical test specimens and strained them to failure uniaxially at a quasi-static strain rate. Intimal failure was determined by videography. The authors of the present study chose to use the porcine data as the foundation for the human carotid artery model, following an observation made by Stemper et al. that young porcine descending aorta samples are likely to be a better surrogate for human arterial data. This observation is based on the following: fresh (not frozen or fixed) porcine samples are easily obtained. Young porcine samples (aged < 6mo.) are readily available whereas human arterial samples are typically of advanced age. The young arterial samples were also generally more elastic, exhibiting a greater strain to intimal failure than the human samples. Histological examination of the two samples found similar intimal pathology.

Converting observed failure values from Stemper et al. from engineering stress and strain to true stress and strain yields values of 2.0 MPa and 49% respectively. Despite observed intimal damage following 25% of the 0.5 m drop tests and 100% of the 0.7 m drop tests, the simulated stress (output from LS-Dyna is true stress) does not exceed this value in any of the simulations (see Table 4). However, the maximum strain resulting from the 0.7 m drop test (46%) approaches this value.

Strain to intimal failure may be a function of the strain rate in the vessel. It is well known that soft tissue is viscoelastic, exhibiting a rate dependent response to loading. The simulation indicates that the average strain rate in the first 5 ms of the guillotine test is 73 strain•sec^{-1}. This strain rate is in the range of previous injury biomechanics research investigating dynamic failure mechanics of arterial specimens. In their 1982 study, Mohan and Melvin used strain rates between 80 to 100 strain•sec^{-1} to investigate the failure properties of human aortic tissue. The investigators found that strain rate did not affect the ultimate strain of the aortic samples. However Mohan and Melvin were investigating ultimate stress not stress to intimal side at subfailure levels. Since Stemper et al. observed that intimal failure nearly always occurs prior to catastrophic failure, the Mohan and Melvin data is likely representative of the adventitial failure properties, and not necessarily those of the intima.

Heretofore, the discussion has centered on how the material characteristics of the vessel may have contributed to the incidence of luminal damage found in the experiments. However, intima to intima contact is another possible mechanism contributing to the 100% incidence of interior lumen damage following the 0.7 m drop. Fluid separation did not occur in the 0.3 m and 0.5 m drop simulations, but Figure 8 shows that contact is present in all simulations. The lumen of the samples was very delicate and could

certainly have been damaged by merely pinching the sides together. While this evidence alone is insufficient to implicate intima to intima contact as a mechanism of carotid artery injury, it is a clear demonstration of insight into the mechanics of the artery during a dynamic event that can only be gained through the use of FEA.

This conclusion shifts focus back to the testing method itself. The purpose of the experiment was to expose the carotid artery samples to sufficient axial tension and "pinching" to illicit internal layer failure. In real world crash scenarios, these two mechanical insults have been identified as mechanisms for carotid artery injury, with tension resulting from hyperextension of the neck and the "pinching" being associated with seat belt impingement on the neck. Clearly this test setup does not mimic the kinematics of the neck interacting with a seat belt, nor is it known how well the foam represents the soft tissue of the neck surrounding the carotid artery, however (and most importantly relative to this study), it is a repeatable test procedure for producing intimal side damage as a function of anvil drop height. The straightforward experimental design lends itself to computational investigation of the stress and strain experienced by the foam-encased artery and therefore is ideally suited for organ level model validation, the purpose of this study.

This organ level validation serves as an intermediate step between modeling the tissue level uniaxial tension tests and modeling the entire organ within a model of yet higher complexity (e.g. full neck model). While still more organ level validation may be required several important observations can be made from these initial simulations. First, the constitutive model of the artery based on uniaxial strain data seems to be a good choice for modeling the mechanical response of the artery. Care must be taken when using a curve fit model to ensure that model strain levels never exceed the maximum value of the stress vs. strain data provided to the model. Post-processing of the model demonstrated that this does not occur. The uniaxial data extends to roughly 55% strain (true), the point of catastrophic vessel failure. Model strains never exceeded 46% in the region below and near the indenter. Peak strain values in the artery for the most injurious drop test (0.7 m) approach strain values published in the literature for intimal side damage. The model is stable, exhibiting low hourglass energy despite large strains and strain rates. With regard to the elevated hourglass energy of the foam, the authors take the stance of previous researchers in the field who have cautioned against using elevated hourglass energy as a stand-alone indicator of model robustness (Takhounts et al. 2003). In our case, in the absence of any indication of model instability we consider the high hourglass to internal energy ratio in the foam a note of caution but not an indication of a serious flaw in the model.

The approach for modeling the fluid in the vessel was shown to be robust. The approach chosen uses LS-Dyna's fluid modeling algorithms employing Lagrangian and Eulerian elements simultaneously. The fluid modeling is based on an equation of state and does not employ full computational fluid dynamic (CFD) solutions. A CFD approach to the problem would add to the computational cost, and the purpose of this study is not to investigate what is happening mechanically within the fluid but to replicate the experimental conditions, and to investigate the mechanics of the artery itself under high rate, and large deformations. The same modeling technique has been used previously in injury biomechanics research in developing a nonlinear model of the eye for investigating globe rupture (Stitzel, Duma et al. 2002).

The experiment used in this organ-level validation study leads to some limitations on the results. The experimental design precludes validation of arterial strains beneath the indenter via tracking markers on the adventitial side. However, with tissue level validation completed prior to this study and with the foam and indenter motion validated against video of the experiment, the strain values calculated in the model are considered valid. Another potentially contentious point of the experiment is the use of a 5 mm beveled indenter in the tests. The experiment was not designed to recreate conditions experienced by a vehicle occupant in any particular crash mode. However it is a repeatable means to creating tensile and pinching loading mechanisms that while exaggerated may be considered "worst case" loading. Specifically regarding the indenter, since a fabric belt will not support compression or bending, in a dynamic event where belt contact on the neck occurs, the authors postulate that the belt may fold back onto itself as the tensile load increases. This folding or "roping" would result in a semicircular shape of relatively small radius, which the authors feel is reasonably represented by the beveled indenter. Roping is generally associated with the lap belt.

A subtle but important aspect of this study is the coding of damage to the inner layer of the artery without using histology. The authors acknowledge that damage to the lumen of the artery characterized as purely intimal would be impossible to determine with the unaided eye. The intima is an extremely thin cellular layer of the vessel wall and microscopic analysis would be required to detect deficits in this layer resulting from testing. However, damage to the intimal side characterized by disruption of the entire intima and a portion of the remaining layers is discernible. We refer again to the work of Stemper et al. (Stemper et al. 2005). In this work, arterial subfailure was correlated to a stress and strain state via videography, not histological analysis. Since we employ data from these tests in our material model, the aim of the study was to use the

FE model results to predict the same type of damage, sub-catastrophic failure involving both the intima and a portion of the remaining vessel wall. The investigation of purely intimal vessel failure is an interesting topic and may be a matter for future research.

A number of researchers have investigated arterial mechanics of the individual layers (Shulze-Bauer, et al. 2003; Fung, 1993). Fung tested specimens of porcine thoracic aorta under bending to determine the mean value of Young's modulus (stiffness) for the intima-media layer and the adventitial layer. His analysis showed that in general, the intimal-medial layer was significantly stiffer than the adventitial layer. Holfzapel et al. described a method to test all three arterial layers individually under quasi-static uniaxial loading by separating layers with a scalpel prior to testing, and reported that the intima is the stiffest layer over the whole domain (Holzapfel, Sommer et al. 2005). This testing however was performed on postmortem human left anterior descending coronary artery samples which have exhibited remarkable intimal thickening. The intima alone in this study was reported as 27% of the total wall thickness. Therefore it is likely that the microscopic composition of what Holzapfel regarded as intima bears little resemblance to healthy intima lining large vessels like the carotid.

Qualitatively, the above findings support the notion that intimal sub failure will nearly always occur prior to catastrophic vessel failure since the adventitia was found to be more compliant than the inner layers. However the data is insufficient for developing finite element models. In the case of the Fung data, only elastic moduli were calculated and in the case of the Holzapfel data, specimen quality is questionable. To the author's knowledge, the uniaxial data from the literature we have employed in tissue level and organ level validation of the carotid artery model is the only data set available that directly links stress and strain values to internal layer failure.

CONCLUSION

We have presented a computational and experimental study on the organ level validation of a fluid filled carotid artery model. The carotid artery model was developed using a simplified rubber model and employs both Lagrangian and Eulerian element formulations. Intimal-medial damage was found with 100% frequency following a drop of a 2.4 kg indenter from a height of 0.7 m. Simulations of this experiment result in maximum true strain levels beneath the indenter of 46%, a value that approaches published data on strain to internal layer failure. The simulations indicate that strain rates as high as 73 strain•sec^{-1} are experienced by the vessel during the event, and that intima to intima contact may have played a role in the frequency of observed damage in the experiment. Insights

gained from this organ level validation will ultimately be used towards the development of a regional level model of the neck.

ACKNOWLEDGEMENTS

The authors gratefully acknowledge Dr. Brian Stemper and Dr. Frank Pintar of the Department of Neurosurgery, Medical College of Wisconsin for the use of data on the failure mechanics of the porcine descending aorta originating from their labs.

The funding for this research has been provided in part by an Australian Research Council linkage grant and by private parties, who have selected Dr. Kennerly Digges and FHWA/NHTSA National Crash Analysis Center at the George Washington University to be an independent solicitor of and funder for research in motor vehicle safety, and to be one of the peer reviewers for the research projects and reports. Neither of the private parties have determined the allocation of funds or had any influence on the content of this report. This research was also supported in part by the Department of Veterans Affairs Medical Research.

REFERENCES

American Heart Association Heart Disease and Stroke Statistics – 2005 Update. Dallas, TX. American Heart Association ; 2005

Biffl, W. L., E. E. Moore, et al. (2001). "Blunt carotid and vertebral arterial injuries." World J Surg **25**(8): 1036-43.

Biffl, W. L., E. E. Moore, et al. (1998). "The unrecognized epidemic of blunt carotid arterial injuries: early diagnosis improves neurologic outcome." Ann Surg **228**(4): 462-70.

Crissey, M. M. and E. F. Bernstein (1974). "Delayed presentation of carotid intimal tear following blunt craniocervical trauma." Surgery **75**(4): 543-9.

Du Bois, P. (2003). A simplified approach for the simulation of rubber like materials under dynamic loading. 4th European LS-DYNA User's Conference, D-I-31/46.

Duck, F. A. (1991). Physical Properties of Tissue, A comprehensive reference book. London, Academic Press.

Fung, Y. (1993). Biomechanics - Mechanical property of living tissue. New York, Springer.

Gayzik, F., J. Tan, et al. (2006). Mesh development for a finite element model of the carotid artery. Biomedical Sciences Instrumentation Rocky Mountian Bioengineering Symposium, Terre Haute, IN.

Haneline, M. T., A. C. Croft, et al. (2003). "Association of internal carotid artery dissection and chiropractic manipulation." Neurologist **9**(1): 35-44.
Haneline, M. T. and G. N. Lewkovich (2005). "An analysis of the etiology of cervical artery dissections: 1994 to 2003." Journal of Manipulative and Physiological Therapeutics **28**(8): 617-622.
Holzapfel, G. A. (2006). "Determination of material models for arterial walls from uniaxial extension tests and histological structure." Journal of Theoretical Biology **238**(2): 290-302.
Holzapfel, G. A., G. Sommer, et al. (2005). "Determination of layer-specific mechanical properties of human coronary arteries with nonatherosclerotic intimal thickening and related constitutive modeling." Am J Physiol Heart Circ Physiol **289**(5): H2048-2058.
Kolling, S., P. Du Bois, et al. (2005). A simplified rubber model with damage. LS-DYNA Anwenderforum, Bamberg.
Lee, J. and K. Yang (2001). "Development of a finite element model of the human abdomen." Stapp Car Crash Journal **45**: 79-100.
LSTC (2003). LS-Dyna Keyword User's Manual, Livermore Software Technology Corporation, April 2003, v. 970.
Miller, P. R., T. C. Fabian, et al. (2001). "Blunt cerebrovascular injuries: diagnosis and treatment." J Trauma **51**(2): 279-85; discussion 285-6.
Miller, P. R., T. C. Fabian, et al. (2002). "Prospective screening for blunt cerebrovascular injuries: analysis of diagnostic modalities and outcomes." Ann Surg **236**(3): 386-93; discussion 393-5.
Mills, N. J. and Y. Masso-Moreu (2005). "Finite Element Analysis (FEA) Applied to Polyethylene Foam Cushions in Package Drop Tests." Packaging Technology and Science **18**: 29-38.
NHTSA (2003). National overview of recent highway safety data. N. H. T. S. Administration.
Reddy, K., M. Furer, et al. (1990). "Carotid artery dissection secondary to seatbelt trauma: case report." J Trauma **30**(5): 630-3.
Richens, D., M. Field, et al. (2004). "A finite element model of blunt traumatic aortic rupture." European Journal of Cardio-Thoracic Surgery **25**(6): 1039-1047.
Rozycki, G. S., L. Tremblay, et al. (2002). "A prospective study for the detection of vascular injury in adult and pediatric patients with cervicothoracic seat belt signs." J Trauma **52**(4): 618-23; discussion 623-4.
Schievink, W. I. (2001). "Spontaneous dissection of the carotid and vertebral arteries." N Engl J Med **344**(12): 898-906.

Schievink, W. I., B. Mokri, et al. (1994). "Recurrent spontaneous cervical-artery dissection." N Engl J Med **330**(6): 393-7.
Shah, C., K. Yang, et al. (2001). "Development of a computer model predict aortic rupture due to impact loading." Stapp Car Crash Journal **45**: 161-182.
Sinson, G. P., N. Yoganandan, et al. (2003). Carotid artery trauma in motor vehicle crashes: Investigation of the local tensile mechanism. IRCOBI Conference, Lisbon, Portugal.
Stemper, B. D., M. R. Stineman, et al. (2005). Mechanical Characterization of Internal Layer Failure in the Human Carotid Artery. IRCOBI, Prauge, Czech Republic.
Stemper, B. D., N. Yoganandan, et al. (2005). "Methodology to study intimal failure mechanics in human internal carotid arteries." J Biomech **38**(12): 2491-6.
Stitzel, J., S. Duma, et al. (2002). "A nonlinear fnite element model of the eye with experimental validation for the prediction of globe rupture." Stapp Car Crash Journal **46**: 243-265.
Stitzel, J., F. Gayzik, et al. (2005). "Development of a finite element based injury metric for pulmonary contusion, Part I: model development and validation." Stapp Car Crash Journal **49**: 271-289.
Takhounts, E., R. Eppinger, et al. (2003). "On the development of hte SIMon finite element head model." Stapp Car Crash Journal **47**: 107-133.
Zhang, L., K. Yang, et al. (2001). "Recent advances in brain injury research: A new human head model development and validation." Stapp Car Crash Journal **45**: 369.

MESH DEVELOPMENT FOR A FINITE ELEMENT MODEL OF THE CAROTID ARTERY

F. Scott Gayzik[1,2], Josh C. Tan[1], Stefan M. Duma[2], Joel D. Stitzel[1,2]

[1]Wake Forest University School of Medicine, Medical Center Blvd, Winston-Salem, NC 27157
[2]Virginia Tech – Wake Forest University Center for Injury Biomechanics, Medical Center Blvd, Winston-Salem, NC 27157

ABSTRACT

A technique for developing a structured, hexahedral and quadrilateral mesh for use in finite element analyses of the carotid artery is presented. The model is reconstructed from 270 Computed Tomography (CT) images (slice thickness 0.625mm) of a 57 year old male subject and extends from the arch of the aorta to the base of the jaw. The structured mesh was generated using an unstructured, automatically generated tetrahedral mesh of the intimal surface of the carotid artery and its branches. A parametric meshing software package was used to create the structured mesh, facilitating mesh density studies. The change in volume and surface area introduced when converting the mesh from tetrahedral to hexahedral elements (+1.5% change in volume, -1.4% change in surface area) is small in comparison to estimated error introduced in the segmentation process. The technique introduced will benefit finite element and fluid dynamic studies of the carotid artery investigating mechanically induced pathology at both physiologic loading rates (i.e., atherosclerotic plaque formation) and high strain rates (i.e., blunt trauma).

Keywords: finite element, mesh, parametric, carotid, hyperelastic, biomechanics

INTRODUCTION

The internal branch of the left and right common carotid arteries along with the vertebral arteries together are responsible for delivering blood to the brain. Disruptions in this blood supply lead to stroke, the third leading killer in the United States. The incidence is rising, and it is estimated 700,000 Americans will become victims of stroke this year. In 2005, the estimated direct and indirect costs of stroke in the United States will reach $56.8 billion[1]. Disruptions of blood flow to the brain can come in the form of a blockage of blood flow (ischemic stroke) or complete structural breakdown of the arteries delivering blood (hemorrhagic stroke).

Of all strokes, 88% are ischemic [1] and of these, atherosclerosis is responsible for more than half. Sites of complex hemodynamics are associated with the formation of atherosclerotic plaques, since the disease is commonly observed at arterial bifurcations and regions of high vessel curvature. These observations have lead to many computational studies seeking to uncover the etiology of the disease by studying mechanical factors such as shear stress, and vessel strain. It is widely accepted that low or oscillatory shear stress contributes to atherogenesis [2]. The wall shear stress temporal gradient, which is of importance due to the pulsatile nature of blood flow, has been related to the expression of atherogenesis-related genes in endothelial cells[3]. Cyclic mechanical strain in the vessel has also been researched extensively. Cyclic strain in endothelial cells and vascular smooth muscle cells is related to elevated synthesis of a potent chemotactic agent for monocytes, leading to lesion development [4].

Not all ischemic strokes are due to atherosclerosis. Spontaneous dissections of the carotid or vertebral artery account for 2% of ischemic strokes but larger percentages of stroke in young or middle aged patients (up to 10 to 25%) [5]. Cervical artery dissection begins as a tear or defect of the intimal lining of the artery, and while uncommon can lead to luminal occlusion and ultimately cerebral ischemia [6]. Internal carotid artery dissection (ICAD) is 3 to 5 times as likely to occur as vertebral artery

dissection, and more than 7000 cases of internal artery dissection per year occur in the United States alone [7-9]. A review of the available literature found that nearly 30% of all ICAD cases are attributed to some form of trauma[6]. Blunt or penetrating carotid artery injures are most commonly encountered in automobile accidents, resulting from interaction with interior structural components of the vehicle or hyperextension and rotation of the head and neck complex [10]. While the incidence of these injuries is low (present in roughly 1% of trauma admissions) the associated mortality and long term neurological morbidity are estimated at 40% and 40-80% respectively [10]. Intimal arterial injury remains the most common initial injury, leading to delayed development of symptoms and diagnosis [11, 12].

Regardless of the etiology of the blood flow disturbance, understanding the complex biomechanics and fluid dynamics of the carotid artery is critical to developing interventions. Finite element analysis (FEA) and computational fluid dynamics (CFD) are widely used in the investigation of arterial mechanics. These techniques lend themselves to investigating the mechanical response at both low (physiologic) and high (traumatic) rates of applied stress and strain. When undertaking a computational study of any system, it is important to know with certainty the material properties, geometry and boundary conditions of that system. Modeling continues to evolve, incorporating sophisticated material models [13], and geometries by using imaging modalities such as MRI and CT. Doppler ultrasound is currently in use to provide more accurate boundary conditions for coupled fluid/solid models [14]. But an important aspect of model development which can lead to spurious results if overlooked is the mesh of the geometry. The mesh refers to how a system is broken into discrete elements which are used in the finite element framework. By and large, the current research in this area is conducted using unstructured meshes composed of tetrahedral elements. This research focuses on the development of a structured, quadrilateral mesh of the carotid artery for use in future research on the biomechanics of the carotid artery.

METHODS

The carotid artery model was constructed from a Computed Tomography (CT) angiography of 57 year old male patient with a history of coronary artery disease with cerebrovascular accident. A bolus of ISOVUE 370 contrast agent was introduced to investigate perfusion through the carotid and cerebral arteries. The carotids were assessed as normal by a qualified radiologist and the image sequence was assumed to representative of an average adult male. Images were taken using a Lightspeed Pro 16 Scanner (GE medical systems, Minneapolis, MN). A total of 270 slices were obtained, from the base of the jaw to the insertion of the artery to the aortic arch. In the sketch of the head and neck complex in Figure 1, the levels of the superior-most and inferior-most scans are depicted by the grey lines. Slice thickness was 0.625 mm and with a resolution of 160 mm x 160 mm. The image size was 512x512 for a resolution of 3.2 pixels/mm or 0.3125 mm per pixel. The images had a grayscale depth of resolution of 16 bits per pixel. The scans were exported to a GE 4.1 Advantage Workstation (GE medical systems, Minneapolis, MN) in DICOM format. Segmentation and thresholding tools were used to extract a region of interest (ROI)

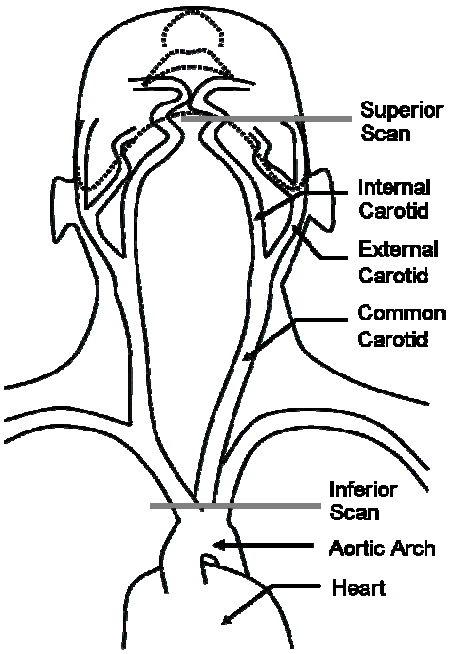

Figure 1. Sketch of head neck complex showing scanned region.

around the left carotid artery from the image stack. The ROI facilitated the subsequent, more detailed segmentation of the arterial lumen.

The lumen of the vessel was segmented using Mimics (Materialise, Leuven, Belgium). Multiple dilation and erosion steps were used to isolate the lumen of the artery. An automatic surface meshing algorithm was used to form a tetrahedral mesh along the intimal surface of the artery. This mesh was exported to TrueGrid (XYZ Scientific Technologies, Inc., Livermore, CA) for hexahedral mesh generation. Splines were drawn circumferentially and longitudinally along the surface of the tetrahedral mesh using existing nodes. Surfaces created from these splines split the carotid model into separate parts which can be meshed parametrically. Parametric meshing is accomplished by mapping each surface of the parts comprising the model to a simple geometric block. The hexahedral mesh is defined on the simplified block and projected back to the complex surfaces of the carotid model. Nodes at the boundaries of the parts composing the parametrically meshed model are then merged.

The structured mesh was imported to LS-PrePost finite element preprocessor (Livermore Software Technology Corp., Livermore, CA) and coated with shell elements. Since the mesh was created by segmenting around the intimal side of the artery, the vessel walls can be modeled with one or more outer layers of shell elements or solid elements.

The geometry data for our work came from scans of a patient at Wake Forest University Baptist Medical Center. All protocols pertaining to confidentiality of patient information, and de-identification of patient data, were strictly followed. The protocol for use of geometry from clinical medical images was reviewed by Wake Forest's Internal Review Board and approved prior to commencement of work.

RESULTS

The entire structured mesh of the carotid artery is shown in Figure 2A. Figure 2B and C show detailed images of the structured mesh and the automatically generated tetrahedral mesh in the region of the bifurcation. The total volume and surface area of the structured mesh matches closely with tetrahedral mesh, see Table 1. The parametric meshing capability of this approach allows for the mesh of the complex structure to be adjusted quickly. Figure 3 demonstrates this capability, showing a cross section of the common carotid artery with the baseline mesh and a mesh with twice the number of elements.

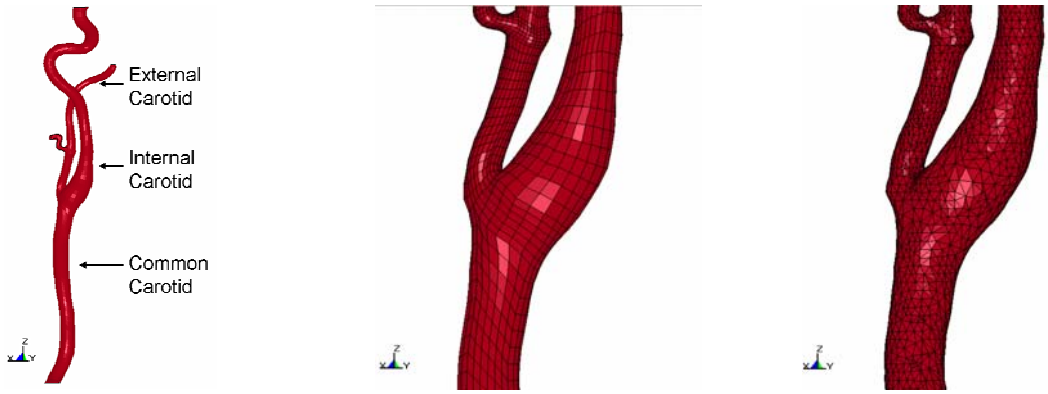

A. B. C.

Figure 2. Results of mesh generation. A. Complete structured mesh of carotid artery. B. Detail of bifurcation, hexagonal mesh. C. Detail of bifurcation, tetrahedral mesh

Table 1. Mesh volume and surface area measurements

	Volume, cm^3	Surface area, cm^2
Hex.	7.59	51.2
Tria.	7.71	51.9
% Diff.	+1.56	-1.35

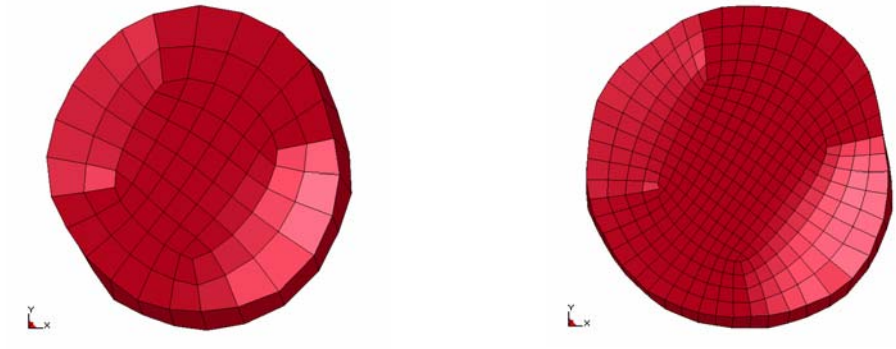

A. B.

Figure 3. Cross section of carotid model showing mesh density. A. Mesh baseline, B. Mesh with double the number of elements

DISCUSSION

A structured mesh of the common carotid artery and its two branches can be a valuable asset in conducting a fluid dynamic or solid mechanic analysis. Since the mesh is created parametrically, the task of refining the mesh density is greatly simplified. Changing the number of elements along any dimension of the model is accomplished simply by changing a parameter and recompiling the input file. Such functionality greatly facilitates analyzing the effect of mesh density on results. It is accepted that models employing structured meshes generally provide more accurate solutions and are more computationally efficient than models employing tetrahedral elements. There are other limitations of tetrahedral meshes when solid mechanics models are concerned; it is possible to encounter material models that are not formulated for use with tetrahedral elements and two-dimensional shells. Using a structured hexahedral mesh with quadrilateral shell elements removes this potential road block.

With any model reconstructed from medical images error is present, however we believe that no significant increase in geometrical error is introduced by meshing the model with hexahedral elements. Error is introduced in each of the three major steps of creating a model; data acquisition, image segmentation, and mesh generation (3-D model construction). Similar studies with roughly the same resolution images have estimated the error due to image segmentation at ±8% in both area and volume. This estimate is based on a ±1 pixel error in segmentation and a roughly circular arterial cross section [14, 15]. Therefore the segmentation error estimate is much larger than the difference in volume and surface area experienced when moving from a tetrahedral to hexahedral mesh (Table 1).

A complete survey of the literature on this subject is beyond the scope of this study. The following brief summary demonstrates that structured meshes are yet to be fully integrated into the most recent works in this area. Coupled fluid/solid models investigating the complex hemodynamics in the area of the carotid bifurcation have widened what is understood regarding plaque formation and rupture [14, 16, 17]. In all of these studies however, unstructured tetrahedral meshes are used in the analysis and several directly cite the complex geometry of the carotid as the reason for using unstructured meshes

[14, 15]. Other studies do employ structured meshes of the bifurcation, but sacrifice geometrical accuracy in the process [18]. A recent study investigated the role atherosclerosis plays in changing the material properties of the vessel wall using the finite element method [19]. While this study employs a structured mesh, the geometry of the model is cylindrical and does not include the bifurcation. No computational models investigating the role blunt trauma to the head neck complex plays in spontaneous carotid artery dissection were found, despite the high incidence of morbidity and neurological deficits associated with this injury. Future research will incorporate material property data into this carotid model. The model will also be placed into a larger model of the neck for use in predicting carotid artery injury in vehicle side impact simulations.

CONCLUSIONS

A method for producing a structured hexahedral and quadrilateral mesh for use in finite element analyses of the human carotid artery is presented. The error introduced in converting from a tetrahedral mesh to a hexahedral mesh is small in comparison to the estimated error introduced during segmentation. The mesh is generated parametrically, facilitating studies of mesh density.

ACKNOWLEDGMENTS

Thanks to Mike Burger for applying his expertise using TrueGrid to the carotid artery model. The funding for this research has been provided in part by an Australian Research Council linkage Grant and by private parties, who have selected Dr. Kennerly Digges and FHWA/NHTSA National Crash Analysis Center at the George Washington University to be an independent solicitor of and funder for research in motor vehicle safety, and to be one of the peer reviewers for the research project and reports. Neither of the private parties have determined the allocation of funds or had any influence on the content of this report.

REFERENCES

[1] A. H. Association, "Heart Disease and Stroke Statistics - 2005 Update," A. H. Association, Ed., 2005.

[2] D. N. Ku, D. P. Giddens, C. K. Zarins, and S. Glagov, "Pulsatile flow and atherosclerosis in the human carotid bifurcation. Positive correlation between plaque location and low oscillating shear stress," *Arteriosclerosis*, vol. 5, pp. 293-302, 1985.

[3] X. Bao, C. Lu, and J. A. Frangos, "Temporal gradient in shear but not steady shear stress induces PDGF-A and MCP-1 expression in endothelial cells: role of NO, NF kappa B, and egr-1," *Arterioscler Thromb Vasc Biol*, vol. 19, pp. 996-1003, 1999.

[4] T. J. Reape and P. H. Groot, "Chemokines and atherosclerosis," *Atherosclerosis*, vol. 147, pp. 213-25, 1999.

[5] W. I. Schievink, "Spontaneous dissection of the carotid and vertebral arteries," *N Engl J Med*, vol. 344, pp. 898-906, 2001.

[6] M. T. Haneline and G. N. Lewkovich, "An analysis of the etiology of cervical artery dissections: 1994 to 2003," *Journal of Manipulative and Physiological Therapeutics*, vol. 28, pp. 617-622, 2005.

[7] M. Giroud, H. Fayolle, N. Andre, R. Dumas, F. Becker, D. Martin, N. Baudoin, and D. Krause, "Incidence of internal carotid artery dissection in the community of Dijon," *J Neurol Neurosurg Psychiatry*, vol. 57, pp. 1443, 1994.

[8] W. I. Schievink, B. Mokri, and W. M. O'Fallon, "Recurrent spontaneous cervical-artery dissection," *N Engl J Med*, vol. 330, pp. 393-7, 1994.

[9] M. T. Haneline, A. C. Croft, and B. M. Frishberg, "Association of internal carotid artery dissection and chiropractic manipulation," *Neurologist*, vol. 9, pp. 35-44, 2003.

[10] B. D. Stemper, N. Yoganandan, and F. A. Pintar, "Methodology to study intimal failure mechanics in human internal carotid arteries," *J Biomech*, vol. 38, pp. 2491-6, 2005.

[11] W. L. Biffl, E. E. Moore, P. J. Offner, and J. M. Burch, "Blunt carotid and vertebral arterial injuries," *World J Surg*, vol. 25, pp. 1036-43, 2001.

[12] A. P. Bok and J. C. Peter, "Carotid and vertebral artery occlusion after blunt cervical injury: the role of MR angiography in early diagnosis," *J Trauma*, vol. 40, pp. 968-72, 1996.
[13] G. A. Holzapfel, T. C. Gasser, and R. W. Ogden, "Comparison of a multi-layer structural model for arterial walls with a fung-type model, and issues of material stability," *J Biomech Eng*, vol. 126, pp. 264-75, 2004.
[14] H. F. Younis, M. R. Kaazempur-Mofrad, R. C. Chan, A. G. Isasi, D. P. Hinton, A. H. Chau, L. A. Kim, and R. D. Kamm, "Hemodynamics and wall mechanics in human carotid bifurcation and its consequences for atherogenesis: investigation of inter-individual variation," *Biomech Model Mechanobiol*, vol. 3, pp. 17-32, 2004.
[15] M. R. Kaazempur-Mofrad, A. G. Isasi, H. F. Younis, R. C. Chan, D. P. Hinton, G. Sukhova, G. M. LaMuraglia, R. T. Lee, and R. D. Kamm, "Characterization of the atherosclerotic carotid bifurcation using MRI, finite element modeling, and histology," *Ann Biomed Eng*, vol. 32, pp. 932-46, 2004.
[16] H. F. Younis, M. R. Kaazempur-Mofrad, C. Chung, R. C. Chan, and R. D. Kamm, "Computational analysis of the effects of exercise on hemodynamics in the carotid bifurcation," *Ann Biomed Eng*, vol. 31, pp. 995-1006, 2003.
[17] Z.-Y. Li, S. Howarth, R. A. Trivedi, J. M. U-King-Im, M. J. Graves, A. Brown, L. Wang, and J. H. Gillard, "Stress analysis of carotid plaque rupture based on in vivo high resolution MRI," *Journal of Biomechanics*, vol. In Press, Corrected Proof.
[18] F. M. Box, R. J. van der Geest, M. C. Rutten, and J. H. Reiber, "The influence of flow, vessel diameter, and non-newtonian blood viscosity on the wall shear stress in a carotid bifurcation model for unsteady flow," *Invest Radiol*, vol. 40, pp. 277-94, 2005.
[19] A. Nagaraj, H. Kim, A. J. Hamilton, J.-H. Mun, B. Smulevitz, B. J. Kane, L. L. Yan, S. I. Roth, D. D. McPherson, and K. B. Chandran, "Porcine carotid arterial material property alterations with induced atheroma: an in vivo study," *Medical Engineering & Physics*, vol. 27, pp. 147-156, 2005.

CHARACTERIZATION OF THE CAROTID AND ADJACENT ANATOMY USING NON-CONTRAST CT FOR BIOMECHANICAL MODEL DEVELOPMENT

Callie C. Lambert, F. Scott Gayzik, Joel D. Stitzel
Wake Forest University School of Medicine

ABSTRACT

The path of the carotid artery and its branches through the neck is characterized through an analysis of non-contrast computed tomography (CT) scans. The distance from the vessel wall of the carotid arteries to the skin and vertebral bodies are recorded from the level of the 2nd cervical vertebrae (C2) to the 6th cervical vertebrae (C6). A total of seven individuals were included in the study. The common carotid artery exhibited the closest average distance to the skin (23.5 ± 6.9 mm) whereas the internal carotid artery exhibited the closest average distance to the vertebral body (7.36 ± 3.8 mm, measured to the transverse process). This study provides morphological validation data towards the development of a regional-level finite element model of the neck and may also be used for the design of biomechanical experiments for the study of carotid artery injury.

Keywords: Carotid artery, modeling, computed tomography, injury, clinical, biomechanics

INTRODUCTION

The majority of blunt carotid artery injuries (CAI) result from motor vehicle crash. [1] While the overall incidence of blunt CAI is low, patients diagnosed with these demonstrate an elevated mortality rate, estimated to be as high as 40%. [2] The diagnosis of CAI has improved in recent years through more aggressive angiographic screening [3], yet many injuries go unrecognized until the onset of neurological symptoms. [4] Injury mechanisms include component contact, and hyperextension and rotation of the head and neck. CAI may result in intimal sub-failure or complications following the formation and release of atherosclerotic plaque in the artery. [2] The location of the insult and the type of loading are likely to play a role the severity of the injury. This is due to structural changes in artery like the main bifurcation, which has been shown to be vulnerable to atherosclerotic plaque formation [5] and because the proximity of the artery to surrounding structures varies as the arteries traverse the neck.

Mitigation of this injury is approached via increased awareness of CAI in the clinic and improved countermeasure design by engineers. One approach to developing improved countermeasures is through computational modeling. Past research on blunt carotid injury has laid the foundation for more complicated modeling efforts. The mechanical properties of the artery at both quasi-static and dynamic rates have been characterized. [6, 7] An organ level finite element (FE) model studying the mechanics of the artery under dynamic loading has been conducted. [8] Thus a regional level FE model incorporating our knowledge of the biomechanics of this vessel is an important research objective. To this end, it is imperative to characterize the location of the carotid artery in the neck, through measurements of the average distance from the carotid to nearby structures. Specifically, this study determines the average distance from the external wall of the carotid artery and its branches to both the skin and nearby vertebral structures. Data from this study will be of use not only in model development, but also for the development of future biomechanical experiments and for the determination of injury mechanisms following real-world CAI.

METHODS

Non-contrast CT scans were obtained for seven individuals (4 male, 3 female) with a GE Lightspeed Plus in Helical Mode with a slice thickness of 2.5 mm. Average age, height and weight of the individuals were 68.8 ± 7.2 years, 171.7 ± 10.9 cm, and 90.5 ± 9.6 kg respectively. Scans were imported into TeraRecon (San Mateo, CA) and viewed through the AquariusNet Viewer, version 1.6.5.1. Patients had no diagnosed arterial injury or abnormal neurological symptoms. The anatomy common to all sets of scans was examined for the seven individuals in this study and determined to be the cervical vertebrae between levels two and six (C2-C6). Using TeraRecon's measurement tool the shortest distance from the external wall of the carotid to the skin was measured for the common, internal, and external carotid arteries and the shortest distance from the external wall of the carotid to the nearest vertebral structure was measured for each of these arteries (Figure 1). Two scans per vertebral body were used to gather measurement data. These were defined by what portion of the transverse process was visible in the particular scan. Measurements were taken at the level in which the transverse process was most visible, and at the level in which the transverse process was least visible. The former would correlate to a superior section of a given vertebral body whereas the latter would correlate to an inferior section. This was repeated for two measurements per vertebrae from C2 through C6 for all 7 patients.

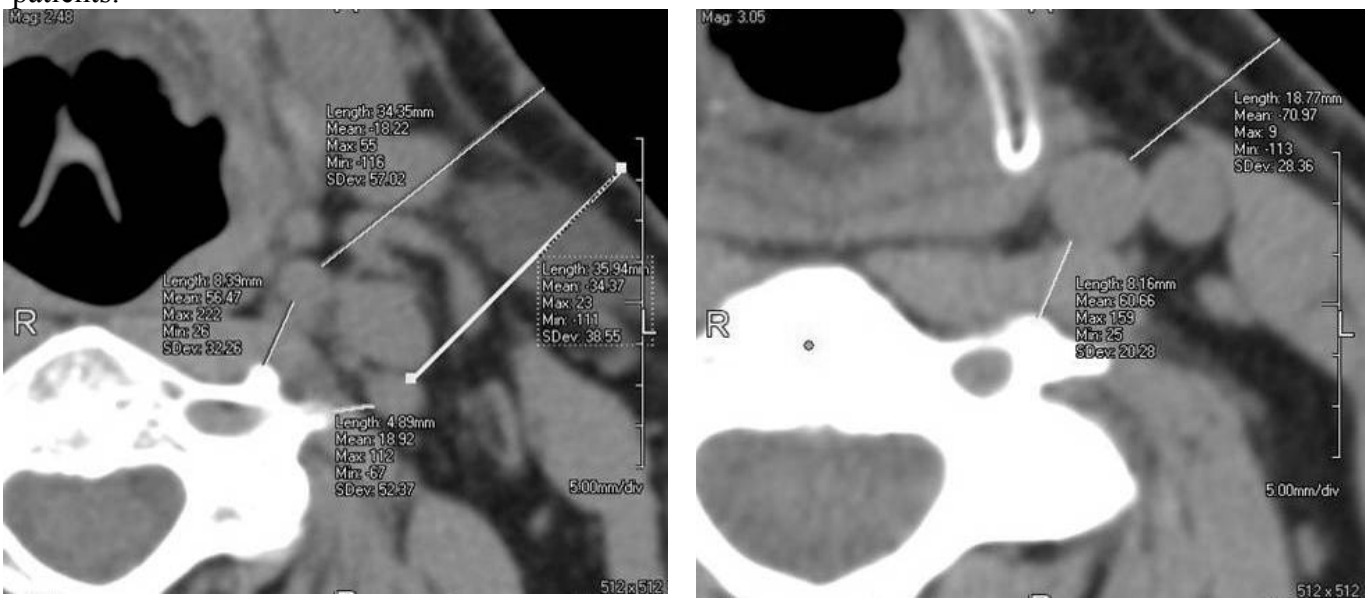

A B

Figure 1: Measurements of Internal and External Carotid (A) and Common Carotid (B) from external wall to nearest vertebral structure and skin. A, P, R and L are Anterior, Posterior, Right and Left. White structure is cervical vertebrae, circular structures indicate vessels.

RESULTS

The results are summarized in Figures 2-4. The average distance from the external wall of the carotid artery to the nearest skin is 33.04 mm. The average distance from the external wall of the carotid artery to the nearest vertebral structure is 8.92 mm. Figure 2 displays the average distance from the common, internal, and external carotid arteries to the nearest skin and vertebral structure, with error bars representing one standard deviation. The results of the shortest distance from the carotid artery to the nearest vertebral structure were also sorted by the type of vertebral structure: the transverse process, vertebral body, facet, and anterior arch. These results are shown in Figure 3. Finally, the average

distance from the carotid artery to the nearest skin and vertebral structure was sorted by level the measurement was taken at to observe how these distances changed with the anatomy of the body. The results are shown in Figure 4.

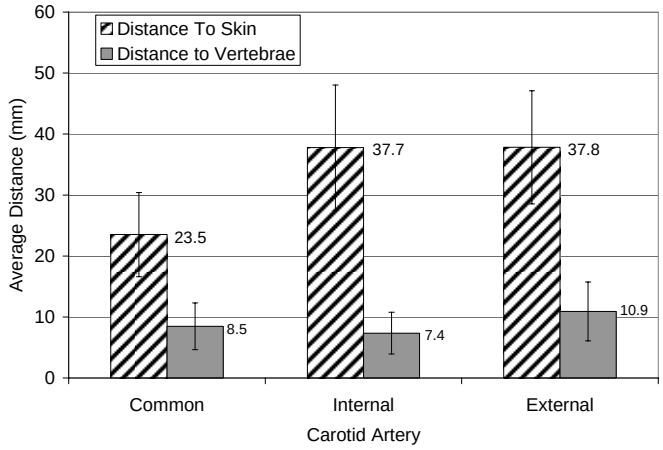

Figure 2: Average distance from carotid artery branches to nearest structure and skin.

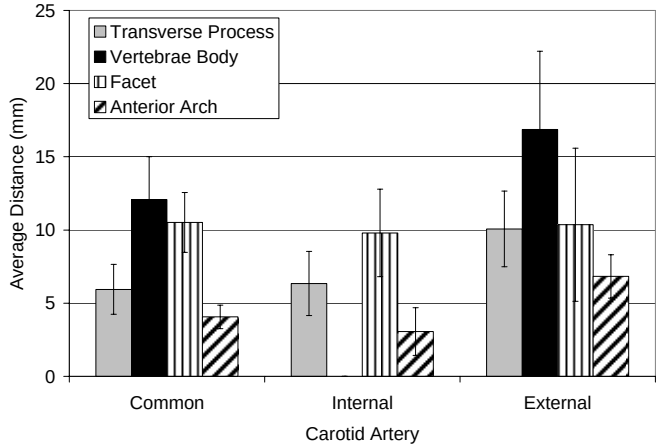

Figure 3: Average distance from carotid artery branch to nearest bone structure

Table 1. Average distance and standard deviation (σ) values from Carotid branches to Skin and Vertebrae (Figure 1)

From	To	Distance, mm	σ, mm
Common Carotid	Skin	23.5	6.9
Internal Carotid		37.8	10.3
External Carotid		37.8	9.3
Common Carotid	Vertebrae	8.5	3.8
Internal Carotid		7.4	3.4
External Carotid		10.9	4.8

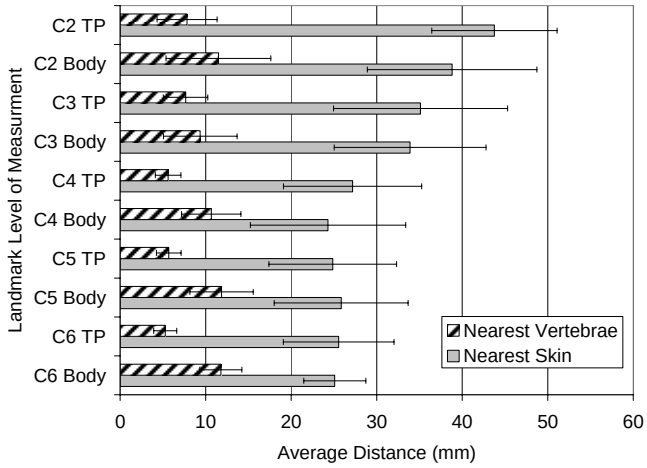

Figure 4: Average distance from artery (all branches) to nearest structure or skin, arranged by cervical vertebrae level. Values are arranged superiorly to inferiorly

Table 2. Distance and standard deviation to nearest structure or skin, arranged by cervical vertebrae level (Figure 3)

		External Carotid to Vertebrae		**External Carotid to Skin**	
		Distance, mm	**σ, mm**	**Distance, mm**	**σ, mm**
C2	Body	9.9	3.3	43.1	6.2
	TP	13.3	7.4	39.6	9.5
C3	Body	9.2	2.4	36.0	10.6
	TP	11.1	4.5	33.4	9.0
		Internal Carotid to Vertebrae		**Internal Carotid to Skin**	
		Distance, mm	**σ, mm**	**Distance, mm**	**σ, mm**
C2	Body	6.0	2.8	44.4	8.6
	TP	9.7	4.3	38.0	11.1
C3	Body	6.1	1.7	34.3	10.5
	TP	7.7	3.6	34.4	9.4
		Common Carotid to Vertebrae		**Common Carotid to Skin**	
		Distance, mm	**σ, mm**	**Distance, mm**	**σ, mm**
C4	Body	5.6	1.5	27.2	8.1
	TP	10.7	3.5	24.3	9.1
C5	Body	5.7	1.4	24.9	7.5
	TP	11.9	3.7	25.8	7.8
C6	Body	5.3	1.3	25.6	6.5
	TP	11.8	2.5	25.1	3.6

DISCUSSION

Characterizing the location of the carotid artery is of importance to both the clinical and impact biomechanics community. Relative to biomechanical studies, the data presented in this work will be useful for computational modeling, experiment design and countermeasure design.

In recent years finite element (FE) analysis has been used to study the mechanics of soft tissues in blunt injury. Studies have focused injuries to specific organs including the brain [9, 10], lung [11], aorta [12], eye [13] and abdomen. [14] This approach has been applied to the carotid artery as well. [8, 15] When developing FE models for blunt impact studies, the preferred paradigm is to add complexity

by working from the tissue, to organ, to regional level. This development strategy provides a structured transition from models that are geometrically simplified and relatively easy to validate to models that are geometrically complex and difficult to validate. At the tissue level the focus is on validating the material model. At the organ level, the geometry of the organ and a simplified loading condition are included. [8] The regional level model incorporates the complexity of the complete system. Thus for a regional carotid artery model, it is insufficient for only the morphology of the artery be accurate, the placement relative to surrounding structures must also be valid. The data presented in this work directly answers this need. Of course a validated regional model would require myriad other modeling considerations such as organ to organ contact definitions, but such considerations are beyond the scope of this study.

This data is of use outside the modeling domain as well. Characterizing the surrounding region is beneficial for designing experiments wherein the results are intended for countermeasure design or model validation. In an organ level experiment using excised porcine carotid arteries, Gayzik et al. situated the artery between two foam layers 15 mm and 25 mm thick (top and bottom respectively) prior to blunt impact. [8] The experiment was designed to elicit a particular injury causation scenario thought to occur in MVC; large axial strain and pinching of the carotid artery. As such, designing the experiment to closely approximate the neck anatomy was secondary to ensuring repeatability and the ability to cause the desired loading conditions. However, in light of the current findings, the 15 mm of foam between the indenter and the vessel represents a thickness roughly between the thickness of the soft tissue medial to and lateral to the artery (Figure 2). Focusing on only the lateral thickness of this protective fascia, the experiments by Gayzik et al. represent a 'worst case scenario' of blunt lateral loading to the neck. Figure 4 shows that the average individual is likely to have protective fascia enveloping the artery in excess of 15 mm. Since the experiment represented a simplified loading condition that focused on restraint belt neck impingement, the effects of the underlying bony geometry were not included. [8] However this data indicates that due to the proximity of the artery to bony structures this aspect of the anatomy should be included in future experimental studies of CAI.

Knowledge of the regional morphology can also aid in the clinical setting. Blunt carotid artery injury most commonly occurs in motor vehicle crash. [2] As such, the National Highway Traffic Safety Administration's (NHTSA) Crash Injury Research and Engineering Network (CIREN) database is an excellent source to investigate the mechanism of injury. Analysis of CIREN cases has led researchers to postulate that localized stretching of the artery secondary to neck extension and rotation is the cause for many such injuries. [16] Figure 4 indicates that that the transverse processes of the vertebral bodies are on average 8.7±3.0 mm from the carotid artery. Such proximity likely influences the amount of the localized stretching in cases of extreme hyperextension and rotation, with the transverse process acting as a lever arm. Knowledge of the relative locations of these structures to the artery in conjunction with accident reconstruction data may someday aid in the early diagnosis of CAI.

The imaging data presented in this study is retrospective and the method presented was devised accordingly. During the data collection for this study, the precise positioning of the patient's head and neck was not controlled. A lack of a precise protocol is a limitation in many retrospective imaging studies. It is particularly common in those concerning CT data since prospective studies are not possible due to the radiation dose associated with CT. In the absence of controlled positioning of the neck, the the simplified approach presented in this paper is adequate for characterization of the carotid and adjacent structures of the neck.

CONCLUSIONS

This study quantifies the regional morphology of the carotid artery relative to surrounding structures. The technique utilized seven non-contrast CT scans of physiologically normal patients to identify the shortest distance from the common, internal and external carotid arteries to the nearest bony structure and to the skin. The arteries are situated closer to the bony structures of the cervical vertebrae than to the skin. These data are intended for both the engineer and clinician for use in prediction of arterial injury, model validation, and experimental design.

ACKNOWLEDGMENTS

This study was supported in part by the Wake Forest University Graduate School of Arts and Sciences Summer Research Opportunities Program (SROP).

REFERENCES

[1] R. F. Cuff and J. H. Thomas, "Pediatric blunt carotid injury from low-impact trauma: a case report and review of the literature," *J Trauma,* vol. 58, pp. 620-3, Mar 2005.

[2] B. D. Stemper, N. Yoganandan, and F. A. Pintar, "Methodology to study intimal failure mechanics in human internal carotid arteries," *J Biomech,* vol. 38, pp. 2491-6, Dec 2005.

[3] R. L. Yong and N. S. Heran, "Traumatic carotid cavernous fistula with bilateral carotid artery and vertebral artery dissections," *Acta Neurochir (Wien),* vol. 147, pp. 1109-13, Oct 2005.

[4] P. R. Miller, T. C. Fabian, T. K. Bee, S. Timmons, A. Chamsuddin, R. Finkle, and M. A. Croce, "Blunt cerebrovascular injuries: diagnosis and treatment," *J Trauma,* vol. 51, pp. 279-85; discussion 285-6, Aug 2001.

[5] H. F. Younis, M. R. Kaazempur-Mofrad, R. C. Chan, A. G. Isasi, D. P. Hinton, A. H. Chau, L. A. Kim, and R. D. Kamm, "Hemodynamics and wall mechanics in human carotid bifurcation and its consequences for atherogenesis: investigation of inter-individual variation," *Biomech Model Mechanobiol,* vol. 3, pp. 17-32, Sep 2004.

[6] B. D. Stemper, M. R. Stineman, N. Yoganandan, F. A. Pintar, G. P. Sinson, and T. A. Gennarelli, "Mechanical Characterization of Internal Layer Failure in the Human Carotid Artery," in *IRCOBI*, Prauge, Czech Republic, 2005, pp. 269-277.

[7] B. D. Stemper, N. Yoganandan, and F. A. Pintar, "Mechanics of arterial subfailure with increasing load rate," *Journal of Biomechanics,* vol. in press, 2006.

[8] F. S. Gayzik, O. Bostom, P. Ortenwall, S. Duma, and J. D. Stitzel, "An experimental and compuational study of blunt carotid artery injury," *Annu Proc Assoc Adv Automot Med,* vol. 50, pp. 13-32, 2006.

[9] E. Takhounts, R. Eppinger, J. Campbell, R. Tannous, E. Power, and L. Shook, "On the development of hte SIMon finite element head model," *Stapp Car Crash Journal,* vol. 47, pp. 107-133, 2003.

[10] L. Zhang, K. Yang, R. Dwarampudi, K. Omori, T. Li, K. Chang, W. Hardy, T. Khalil, and A. King, "Recent advances in brain injury research: A new human head model development and validation," *Stapp Car Crash Journal,* vol. 45, p. 369, 2001.

[11] J. Stitzel, F. Gayzik, J. Hoth, J. Mercier, H. M. Gage, K, S. Duma, and R. Payne, "Development of a finite element based injury metric for pulmonary contusion, Part I: model development and validation," *Stapp Car Crash Journal,* vol. 49, pp. 271-289, 2005.

[12] C. Shah, K. Yang, W. Hardy, H. Wang, and A. King, "Development of a computer model predict aortic rupture due to impact loading," *Stapp Car Crash Journal,* vol. 45, pp. 161-182, 2001.

[13] J. Stitzel, S. Duma, J. Cormier, and I. Herring, "A nonlinear fnite element model of the eye with experimental validation for the prediction of globe rupture," *Stapp Car Crash Journal,* vol. 46, pp. 243-265, 2002.

[14] J. Lee and K. Yang, "Development of a finite element model of the human abdomen," *Stapp Car Crash Journal,* vol. 45, pp. 79-100, 2001.

[15] F. S. Gayzik, J. Tan, S. Duma, and J. D. Stitzel, "Mesh development for a finite element model of the carotid artery," *Biomed Sci Instrum,* vol. 42, pp. 187-92, 2006.

[16] G. P. Sinson, N. Yoganandan, F. A. Pintar, R. Morgan, D. Maiman, K. Brasel, and T. A. Gennarelli, "Carotid artery trauma in motor vehicle crashes: Investigation of the local tensile mechanism," in *IRCOBI Conference*, Lisbon, Portugal, 2003, pp. 207-216.

FOREARM FRACTURE BENDING RISK FUNCTION FOR THE 50th PERCENTILE MALE

Anthony C. Santago[1], Joseph M. Cormier[1], Stefan M. Duma[1], Narayan Yoganandan[2], Frank A. Pintar[2]

[1]Virgina Tech – Wake Forest University Center for Injury Biomechanics, Blacksburg VA, 24061

[2]Medical College of Wisconsin, Milwaukee, Wisconsin 53226

ABSTRACT

The increase in upper extremity injuries in automobile collisions, because of the widespread implantation of airbags, has lead to a better understanding of forearm injury criteria. Risk functions for upper extremity injury that can be used in instrumented upper extremities would be useful. This paper presents a risk function for forearm injury for the 50th percentile male based on bending fracture moment data gathered from previous studies. The data was scaled using two scaling factors, one for orientation and one for mass, and the Weibull survival analysis model was then used to develop the risk function. It was determined that a 25% risk of injury corresponds to an 82 Nm bending load, a 50% risk of injury corresponds to a 100 Nm bending load, and a 75% risk of injury corresponds to a 117 Nm bending load. It is believed the risk function can be used with an instrumented upper extremity during vehicle testing.

Keywords: forearm, fracture, male, criteria, bending, airbag, automobile, upper extremity

INTRODUCTION

The advent of airbags has reduced fatal injuries in automobile crashes, but airbags have increased the incidence of certain non-fatal injuries especially those in the upper extremities. It is suggested that the risk of serious upper extremity injury to belted occupants with airbags increases by 40 % when compared to those without airbags [1]. Kuppa et al. showed that 1.1% of drivers who were restrained by a 3 point belt experience upper extremity injuries versus 4.4% of drivers who were restrained by the deploying air bag and 3-point belt experience upper extremity injury [2].

More recently, Jernigan et al. investigated severe upper extremity injuries resulting from frontal automobile crashes to determine the effects of frontal airbags [3]. The National Automotive Sampling System database files from 1993 to 2000 were examined in a study that included 25,464 individual cases that occurred in the United States. An analysis of the cases indicated that occupants exposed to an airbag deployment were statistically more likely to sustain a severe upper extremity injury (2.7%), than those occupants not exposed to an airbag deployment (1.6%) ($p=0.01$). In particular, 0.7% of occupants exposed to an airbag deployment sustained a severe upper extremity injury specifically from the airbag [4].

Two modes of injury have been suggested to explain the increased incident of upper extremity injuries with airbag deployment [5]. The first type is an indirect type of injury in which the airbag propels the upper extremity into an object in the vehicle such as the roof or B-pillar. The second type is called primary contact, which describes injuries directly attributed to contact with the airbag or airbag flap. The primary contact

mechanism has been associated with the more severe forearm fractures, while the indirect mechanism is typically associated with metacarpal injuries [6].

Hardy et al., through experiments, were able to recreate forearm fractures seen in real world cases and were able to discover that forearm velocity was a predictor of injury [7]. Bass et al. found that a forearm bending moment of 67 Nm in the SAE fully instrumented fifth percentile female upper extremity corresponded to a 50% risk of one fracture in either the ulna or radius [5]. Pintar et al. tested male cadaver forearms and was able to find a mean forearm bending moment of 113 Nm [8]. Duma et al. found a mean forearm bending moment of 126 Nm with the arm in supinated position and a mean forearm bending moment of 108 Nm with the arm in the pronated position [9].

The purpose of this study was to combine experimental data from tests that calculated mean forearm failure bending moment and produce a forearm injury risk function for the 50^{th} percentile male by using mass and orientation scaling factors.

METHODS

Data from a total of 28 experiments on male cadaver forearms were gathered from primary studies [8], [9]. Two scaling processes were utilized before the data was input for a risk function. Since the forearm has been shown to be weaker in the pronated position, all supinated tests were scaled down by 14% which was the difference between matched pair tests [9]. Next, the moment was mass scaled, using the entire cadaver, to 77kg which corresponds to the mass of a 50^{th} percentile male [10]. Rate scaling was not needed because the data gathered had equivalent dynamic rates and bones do not become infinitely stronger as the strain rate becomes faster. Pintar et al. showed that there was no statistical difference between 3.3 m/s and 7.6m/s [8].

Survival analysis was utilized to develop the risk functions. A Weibull model was chosen because of its increasing hazard model with severity and the closed form solution of its Cumulative Distribution Function (CDF) [11]. The Weibull CDF is given by, (Equation 1), where λ and γ are the scale and shape parameters respectively and x is the measured bending moment. This function provides an estimate of risk of injury using the maximum likelihood estimate of the scale and shape parameters [12], [13]. A flowchart is shown in Figure 1 that represents the process used to gather and scale the data.

$$\text{Risk of fracture} = 1 - e^{-(\lambda * x)^{\gamma}} \qquad \text{(Equation 1)}$$

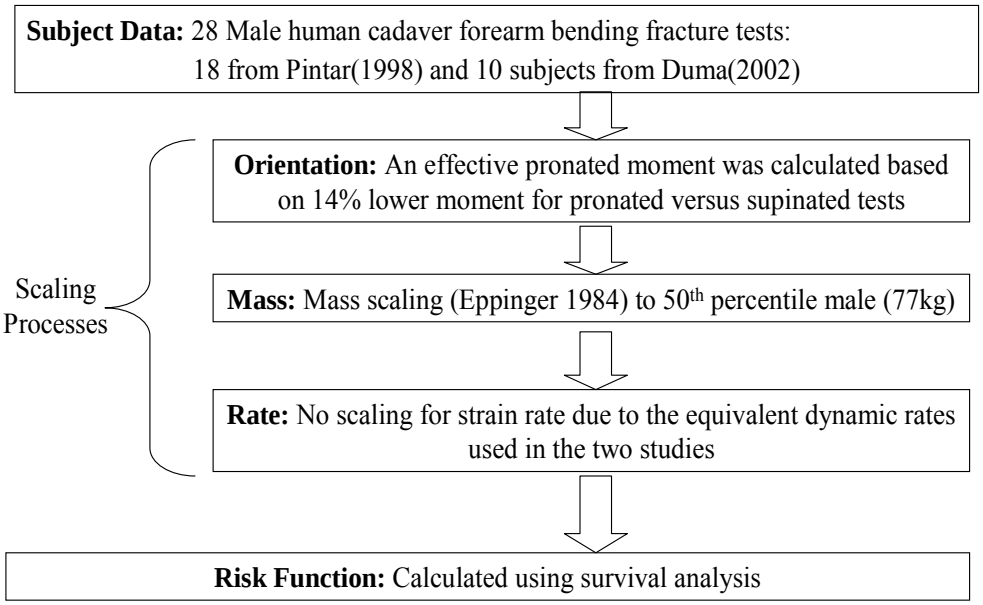

Figure 1: Outline of forearm injury risk function creation process for 50th percentile male.

RESULTS

The original experimental data, as well as the effective scaled moments, are presented in Table 1. Mass scaled moment represents the final scaled failure bending moment used for the risk function. The risk function is shown in Figure 2 and is calculated from equation 2. From the risk function it can be determined that the risk of injury is as follows:

- 5% Risk = 48Nm
- 25% Risk = 82Nm
- 50% Risk = 100Nm
- 75% Risk = 117Nm
- 95% Risk = 165Nm

$$\text{Risk of forearm fracture} = 1 - e^{-(0.0092 * x)^{4.409}} \quad \text{(Equation 2)}$$

Table 1: Forearm fracture data for each male used in risk function calculation.

Paper	Test Number	Age	Body Mass	Moment	Orientation	Effecitive Pronanted Moment	Mass and Orientation Scaled Moment
		(years)	(kg)	(Nm)	Orientation	(Nm)	(Nm)
Duma 2002	1	50	63.5	116	supinated	100	122
Duma 2002	2	57	99.9	109	supinated	94	73
Duma 2002	3	48	80.3	141	supinated	121	117
Duma 2002	4	60	72.1	132	supinated	113	122
Duma 2002	5	63	70	132	supinated	113	126
Duma 2002	6	50	63.5	102	pronated	102	125
Duma 2002	7	57	99.9	99	pronated	99	77
Duma 2002	8	48	80.3	118	pronated	118	114
Duma 2002	9	60	72.1	114	pronated	114	123
Duma 2002	10	63	70	107	pronated	107	119
Pintar 1997	1	41	87	76.5	supinated	66	59
Pintar 1997	2	74	90	163.2	supinated	140	121
Pintar 1997	3	74	79.4	119.2	supinated	102	100
Pintar 1997	4	44	124.7	186	supinated	160	99
Pintar 1997	5	72	68	48.3	supinated	41	47
Pintar 1997	6	41	90	130	supinated	112	96
Pintar 1997	7	69	79.4	142.5	supinated	122	120
Pintar 1997	8	66	68	87.1	supinated	75	85
Pintar 1997	9	66	124.7	178.9	supinated	153	96
Pintar 1997	10	72	87	142.1	supinated	122	109
Pintar 1997	11	69	81.6	101.7	supinated	87	83
Pintar 1997	12	68	70.3	76	supinated	65	72
Pintar 1997	13	78	47.6	112.5	supinated	97	158
Pintar 1997	14	44	97.5	99	supinated	85	68
Pintar 1997	15	68	81.6	101.4	supinated	87	83
Pintar 1997	16	78	70.3	68.6	supinated	59	65
Pintar 1997	17	61	47.6	78.3	supinated	67	110
Pintar 1997	18	61	97.5	118.6	supinated	102	81
Mean	N/A	60.8	80.9	114.3	N/A	100.8	98.9
STD	N/A	11.3	18.4	31.8	N/A	27.4	25.8

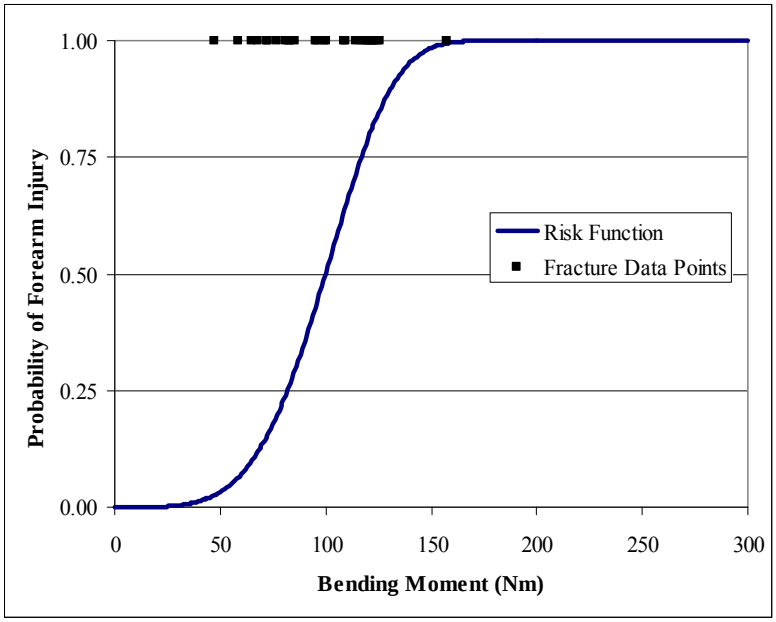

Figure 2: Forearm fracture risk function for the 50th percentile male.

DISCUSSION

Twenty-three of the twenty-eight forearms were tested in the pronated position which causes the resulting risk function to be highly dependent on the 14% orientation scaling factor. Since the scaling factor is developed from five match paired cadaver arms, the accuracy of the scaling factor is a concern but the testing from Duma et al. does show there is a difference in strength between the pronated and supinated position [9]. To create a conservative risk function this difference must be taken into account and those five matched pair tests are represent the best way to scale the data. Without scaling the data the risk function would not predict enough injuries.

Pintar et. al show that the risk of forearm fracture is highly correlated to bone mineral density (BMD) and forearm mass; however, BMD and forearm mass are not know for all test subjects so body mass was used to scale the data [8]. It can be assumed that as body mass increases forearm mass increases proportionately [4], [14].

The study does not take into effect combined loading on the forearm bones. This is a place the study falls short; however, three point bending does have an application if the drivers are extended to the steering wheel and are struck by an airbag.

Duma et al. showed that the 5th percentile female had a 50% risk of injury that corresponded with a 58 Nm bending load [4]. This bending load is more than 40% lower than the 50% risk of injury bending load for the 50th percentile male. This large discrepancy in results demonstrates the need for multiple upper extremity models for automobile occupants because each model will react differently to bending loads applied by the airbags.

CONCLUSION

Based on the experimental data collected from previous primary studies [8], [9] a risk function was computed for the 50th percentile male. The 50th percentile male was chosen because that model is most often used in industry testing. The results show that a 25% risk of injury corresponds to an 82 Nm bending load, a 50% risk of injury corresponds to a 100 Nm bending load, and a 75% risk of injury corresponds to a 117 Nm bending load. It is believed the risk function can be used with an instrumented upper extremity during vehicle testing.

REFERENCES

[1] National Highway Traffic Safety Administration, "Third Report to Congress: Effectiveness of Occupant Protection Systems and Their Use," U.S. *Department of Transportation*, December 1996.

[2] Kuppa, S. M., Yeiser, C. W., Olson, M. B., Taylor, L., Morgan, R., and Eppinger, R., "RAID -An investigation tool to study air bag/upper extremities," *SAE paper* 970399, 1997.

[3] Jernigan, M., Duma, S., "The Effects of Airbag Deployment on Severe Upper Extremity Injuries in Frontal Automobile Accidents," *American Journal of Emergency Medicine*, vol 21 Issue 2 pp 100-105, March 2003.

[4] Duma, S, Boggess B., Bass C., Crandall, J., "Injury Risk Functions for the 5th Percentile Female Upper Extremity," *Stapp Car Crash Conference Proceedings*, *SAE Paper* 2003-01-0166, 2003

[5] Bass, C. et al., "The interaction of air bags with upper extremities", *Proc. 41st Stapp Car Crash Conference*, pp. 101-110, Society of Automotive Engineers, Warrendale, PA, *SAE paper* 973324, 1997
[6] Huelke, D. F., Ryan, G, Schneider, L. W., "Upper extremity injuries from steering wheel airbag deployments," *SAE International Congress and Exposition*, Detroit, Michigan, *SAE paper* 970493, 1997
[7] Hardy, W. N., Schneider, L. W., Reed, M. P., Ricci, L. L., "Biomechanical investigation of airbag induced upper extremity injuries," *41st Stapp International Car Crash Conference*, Orlando, Florida, 1997.
[8] Pintar, F.A., Yoganandan, N., Eppinger, R.H., "Response and tolerance of the human forearm to impact loading," *42nd Stapp International Car Crash Conference*, Temple, Arizona, *SAE paper* 983149, 1998.
[9] Duma, S.M., Schreiber P. H., McMaster, J. D., Crandall, J. R., Bass, C. R., "Fracture tolerance of the male forearm: the effect of pronation versus supination," *Proc Instn Mech Engrs* Vol 216 Part D: Journal of Automobile Engineering May 2002.
[10] Eppinger, R.H., Marcus, J.H., Morgan, R.M., "Development of Dummy and Injury Index for NHTSA's Thoracic Side Impact Protection Research Program," *SAE paper* 840885, 1984
[11] Lee, E.T., Wang, J.W., Statistical Methods for Survival Data Analysis 3rd. John Wiley, New Jersey, 1993.
[12] Allison, P.D., Survival Analysis Using SAS: A Practical Guide, SAS Press, North Carolina, 1995.
[13] Cantor, A.B., Survival Analysis Techniques for Medical Research 2nd, SAS Press, Cary NC, 2003.
[14] Kirkish S. L., Begeman, P. C., Paravasthu, N. S., "Proposed Provisional Reference Values for the Humerus for Evaluation of Injury Potential, Society of Automotive Engineering, Warrendale, PA, *SAE paper* 962416, 1996.

HUMERUS FRACTURE BENDING RISK FUNCTION FOR THE 50th PERCENTILE MALE

Anthony C. Santago, Joseph M. Cormier, Stefan M. Duma
Virginia Tech – Wake Forest University Center for Injury Biomechanics
Blacksburg VA, 24061

ABSTRACT

The increase in upper extremity injuries in automobile collisions, because of the widespread implantation of airbags, has lead to an increased focus in humerus injury criteria. Risk functions for upper extremity injury that can be used in instrumented upper extremities would be useful. This paper presents a risk function for humerus injury for the 50th percentile male based on bending fracture moment data gathered from previous studies. The data was scaled using two scaling factors, one for mass and one for rate, and the Weibull survival analysis model was then used to develop the risk function. It was determined that a 25% risk of injury corresponds to a 214 Nm bending load, a 50% risk of injury corresponds to a 257 Nm bending load, and a 75% risk of injury corresponds to a 296 Nm bending load. It is believed the risk function can be used with an instrumented upper extremity during vehicle testing.

Keywords: humerus, fracture, male, criteria, bending, upper extremity, airbag, automobile, driving, injury

INTRODUCTION

The advent of airbags in automobiles has reduced fatal injuries in automobile crashes, but have increased the incidence of some non-fatal injuries especially those in the upper extremities. It has been suggested that the risk of serious upper extremity injury to belted occupants with airbags increases by 40 % when compared to those without airbags [1]. Kuppa et al. showed that 1.1% of drivers who were restrained by a 3 point belt experience upper extremity injuries versus 4.4% of drivers who were restrained by the deploying air bag and 3-point belt experience upper extremity injury [2].

More recently, Jernigan et al. investigated severe upper extremity injuries resulting from frontal automobile crashes [3]. The National Automotive Sampling System database files from 1993 to 2000 were examined in a study that included 25,464 individual cases that occurred in the United States. An analysis of the cases indicated that occupants exposed to an airbag deployment were statistically more likely to sustain a severe upper extremity injury (2.7%), than those occupants not exposed to an airbag deployment (1.6%) ($p=0.01$). In particular, 0.7% of occupants exposed to an airbag deployment sustained a severe upper extremity injury specifically from the airbag. In addition, when in crashes with an airbag deployment, older occupants were at a higher risk for severe upper extremity injury, as well as occupants in crashes with higher changes in velocity [4].

Two modes of injury have been suggested to explain the increased incident of upper extremity injuries with airbag deployment [5]. The first type is an indirect type of injury in which the airbag propels the upper extremity into an object in the vehicle such as the roof or B-pillar. The second type is called primary contact, which describes injuries directly attributed to contact with the airbag or airbag flap.

Kallieris et al., who used the Hybrid III 50th male dummy and male cadavers, found one humerus fracture out of five cadaver tests and showing an average failure bending moment of 138 Nm for the humerus [6]. Duma et al. , utilizing 12 female cadavers, showed an average bending moment of 128 N m for a 5th percentile female humerus [7]. Kirkish et al., showed an average failure bending moment of 158 Nm for the males that were tested [8].

The purpose of this study was to combine experimental data from tests that calculated mean humerus failure bending moment and produce a humerus injury risk function for the 50th percentile male by using mass and rate scaling factors.

METHODS

Data from a total of 25 three point bending experiments on male cadaver humeri were gathered from two primary studies [6], [8]. Given the symmetry of the humerus, all bending and orientations were considered equal. Moreover, Kirkish et al. found this to be statistically correct [8]. Next, the moment was mass scaled, using the entire cadaver, to 77kg which corresponds to the mass of a 50th percentile male [10]. Given the widely varying impact rates between the tests, the moments were scaled to the equivalent velocity of 3.63 meters/second loading rate because it matches the humerus loading rates as measured in the cadaveric subjects under side airbag loading [7]. This method assumes a linear relationship between impactor velocity and strain rate. A limit was placed on this scaling in that everything below 0.005m/s was treated as 0.005m/s because if the test get infinitely slower the bone does not get infinitely weaker.

Survival analysis was utilized to develop the risk functions. A Weibull model was chosen because of its increasing hazard model with severity and the closed form solution of its Cumulative Distribution Function (CDF) [9]. The Weibull CDF is given by, (Equation 1), where λ and γ are the scale and shape parameters respectively and x is the measured bending moment. This function provides an estimate of risk of injury using the maximum likelihood estimate of the scale and shape parameters [10], [11]. A flowchart is shown in Figure 1 that describes the process for gathering the data and creating the risk function.

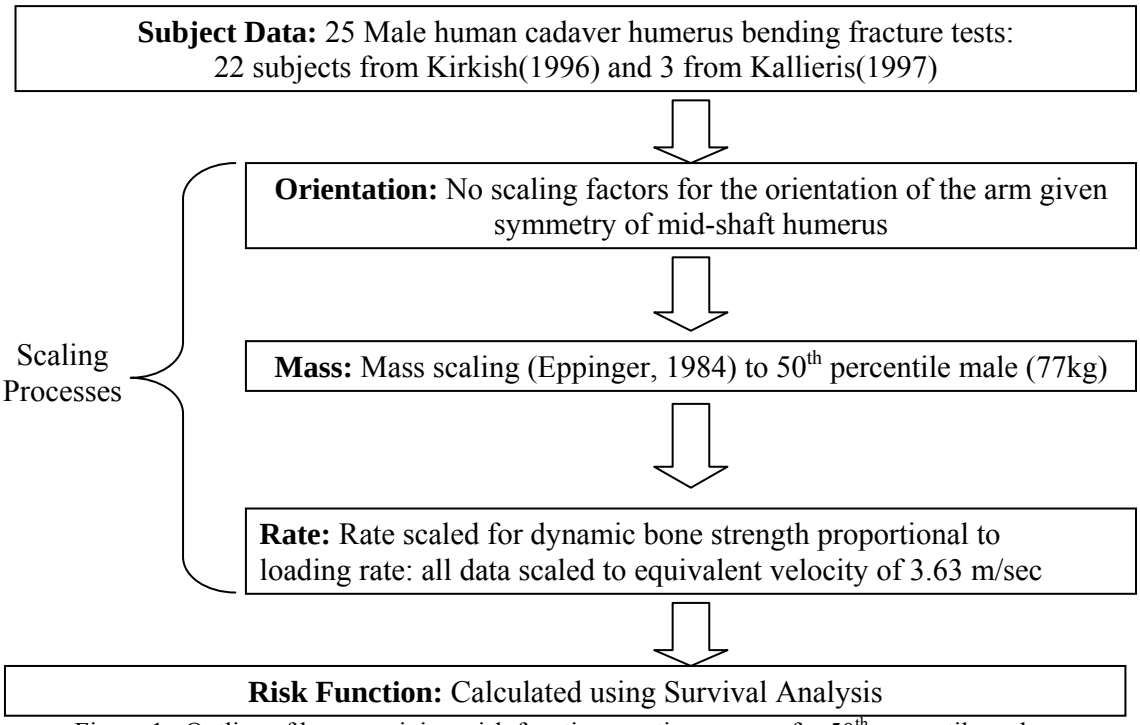

Figure 1: Outline of humerus injury risk function creation process for 50th percentile male.

$$\text{Risk of fracture} = 1 - e^{-(\lambda * x)^{\gamma}} \qquad \text{(Equation 1)}$$

RESULTS

The original experimental data, as well as the effective scaled moments, are presented in Table 1. Rate scaled moment represents the final scaled failure bending moment used for the risk function. The risk function is shown in Figure 2 and is calculated from equation 2. From the risk function it can be determined that the risk of injury is as follows:

- 5% Risk = 151Nm
- 25% Risk = 214Nm
- 50% Risk = 257Nm
- 75% Risk = 296Nm
- 95% Risk = 346Nm

$$\text{Risk of humerus fracture} = 1 - e^{-(0.0036 * x)^{4.871}} \qquad \text{(Equation 2)}$$

Table 1: Humerus fracture data for each male used in risk function calculation.

Paper	Test	Age	Body Mass	Original moment	Test Rate	Mass Scaled Moment	Rate and Mass Scaled moment
		(years)	(kg)	(Nm)	(m/s)	(Nm)	(Nm)
Kirkish 1996	1	66	55.3	149	0.218	209	248
Kirkish 1996	2	66	55.3	182	0.0025	256	380
Kirkish 1996	3	59	58.5	106	0.000635	141	209
Kirkish 1996	4	59	58.5	118	0.218	157	186
Kirkish 1996	5	67	65.3	102	0.000635	121	180
Kirkish 1996	6	69	86.6	240	0.000635	215	320
Kirkish 1996	7	69	86.6	247	0.218	222	262
Kirkish 1996	8	61	75.7	151	0.218	155	183
Kirkish 1996	9	61	75.7	104	0.000635	107	158
Kirkish 1996	10	75	78.9	123	0.000635	121	180
Kirkish 1996	11	75	78.9	145	0.218	143	169
Kirkish 1996	12	66	56.2	150	0.218	207	246
Kirkish 1996	13	66	56.2	151	0.000635	209	310
Kirkish 1996	14	45	81.6	190	0.000635	181	269
Kirkish 1996	15	61	59.4	110	0.000635	144	214
Kirkish 1996	16	61	59.4	148	0.218	194	229
Kirkish 1996	17	61	53.5	150	0.000635	218	323
Kirkish 1996	18	48	56.2	187	0.218	259	306
Kirkish 1996	19	59	47.2	133	0.000635	219	325
Kirkish 1996	20	59	47.2	160	0.218	263	312
Kirkish 1996	21	50	79.4	216	0.218	211	250
Kirkish 1996	22	50	79.4	211	0.218	206	244
Kallieris 1997	C3	69	56	148	0.00025	205	305
Kallieris 1997	C4	86	60	135	0.00025	175	260
Kallieris 1997	C5	45	55	130	0.00025	184	273
Mean	N/A	62.1	64.9	155.4	N/A	188.9	253.6
STD	N/A	9.7	12.5	40.6	N/A	43.5	59.2

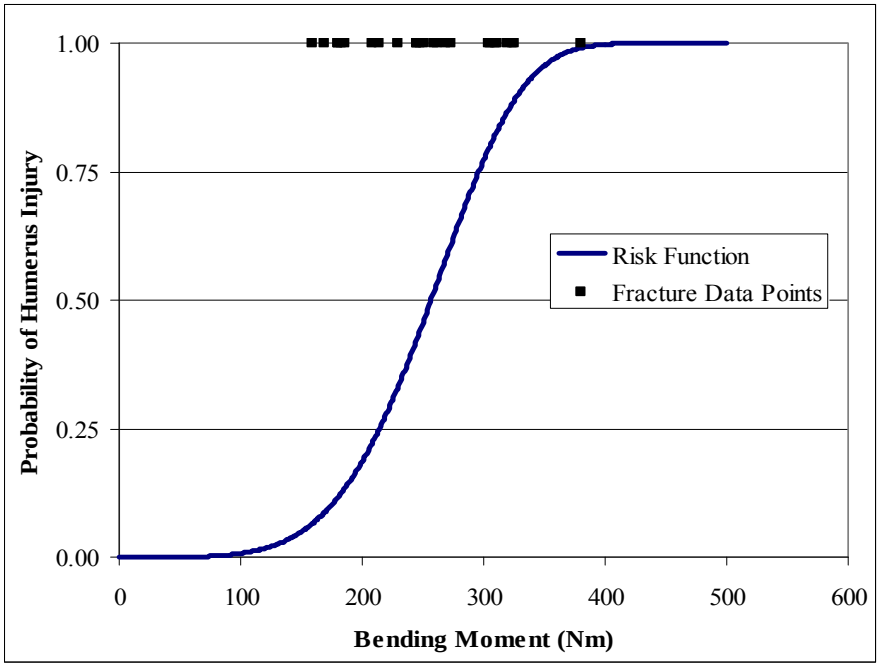

Figure 2: Humerus fracture risk function for the 50th percentile male.

DISCUSSION

Duma et al. showed that the 5th percentile female had a 50% risk of injury that corresponded with a 128 Nm bending load [4]. That bending load is 50% lower than the bending load that corresponds to a 50% risk of injury for the 50th percentile male. This large discrepancy in results demonstrates the need for multiple upper extremity models for automobile occupants because each model will react differently to bending loads applied by the airbags.

Kirkish et al. showed a Lateral-Medial 50th Percentile normalized average fracture force of 236Nm and a Anterior-Posterior 50th Percentile normalized average fracture force of 223Nm [8]. This data, although not normalized for velocity, is comparable to the load calculated for 50% risk of fracture.

CONCLUSION

Based on the experimental data collected from previous primary studies [6], [8] a risk function was computed for the 50th percentile male. The 50th percentile male was chosen because that model is most often used in industry testing. The results show that a 25% risk of injury corresponds to a 214 Nm bending load, a 50% risk of injury corresponds to a 257 Nm bending load, and a 75% risk of injury corresponds to a 296 Nm bending load. It is believed the risk function can be used with an instrumented upper extremity during vehicle testing.

REFERENCES

[1] National Highway Traffic Safety Administration, Third Report to Congress: Effectiveness of Occupant Protection Systems and Their Use, U.S. Department of Transportation, December 1996.

[2] Kuppa, S. M., Yeiser, C. W., Olson, M. B., Taylor, L., Morgan, R., and Eppinger, R., "RAID -An investigation tool to study air bag/upper extremities," *SAE paper* 970399, 1997.

[3] Jernigan, M., Duma, S., "The Effects of Airbag Deployment on Severe Upper Extremity Injuries in Frontal Automobile Accidents," *American Journal of Emergency Medicine*, vol 21 Issue 2 pp 100-105, March 2003.

[4] Duma, S, Boggess B., Bass C., Crandall, J., "Injury Risk Functions for the 5th Percentile Female Upper Extremity," *Stapp Car Crash Conference Proceedings*, *SAE Paper* 2003-01-0166, 2003.

[5] Bass, C., Duma, S., Crandall, J., Morris, R., Pilkey, W., Hurwitz, S., Khaewpong, N., Eppinger, R., et al., "The interaction of air bags with upper extremities", *Proc. 41st Stapp Car Crash Conference*, pp. 101-110, Society of Automotive Engineers, Warrendale, PA, *SAE Paper* 973324, 1997

[6] Kallieris, D., Rizzetti, A., Jost, S., Priemer, P., Unger., M., "Response and Vulnerability of the Upper Arm Through Side Airbag Deployment," *Proc. 41st Stapp Car Crash Conference*, pp. 101-100, Society of Automotive Engineers, Warrendale PA, 1997

[7] Duma, S.M., Schreiber, P.H., McMaster, J.D., Crandall, J.R., Bass, C.R., Pilkey, W.D., "Dynamic Injury Tolerance for Long Bones in the Female Upper Extremity," *Journal of Anatomy*, vol 194, Part 3, pp. 463-71, 1999.

[8] Kirkish S. L., Begeman, P. C., Paravasthu, N. S., "Proposed Provisional Reference Values for the Humerus for Evaluation of Injury Potential, Society of Automotive Engineering, Warrendale, PA, *SAE paper* 962416, 1996.

[9] Lee, E.T., Wang, J.W., Statistical Methods for Survival Data Analysis 3rd. John Wiley, New Jersey, 1993.

[10] Allison, P.D., Survival Analysis Using SAS: A Practical Guide, SAS Press, North Carolina, 1995.
[11] Cantor, A.B., Survival Analysis Techniques for Medical Research 2nd, SAS Press, Cary NC, 2003.